DERIVATION AND ANALYSIS OF NEAR FIELD TO FAR FIELD TRANSFORMATION ALGORITHM FOR SPHERICAL SCANNING

A THESIS SUBMITTED TO
THE GRADUATE SCHOOL OF NATURAL AND APPLIED SCIENCES
OF
MIDDLE EAST TECHNICAL UNIVERSITY

BY

HÜLYA KORKMAZ

IN PARTIAL FULFILLMENT OF THE REQUIREMENTS
FOR
THE DEGREE OF MASTER OF SCIENCE
IN
ELECTRICAL AND ELECTRONICS ENGINEERING

SEPTEMBER 2019

Approval of the thesis:

DERIVATION AND ANALYSIS OF NEAR FIELD TO FAR FIELD TRANSFORMATION ALGORITHM FOR SPHERICAL SCANNING

submitted by **HÜLYA KORKMAZ** in partial fulfillment of the requirements for the degree of **Master of Science in Electrical and Electronics Engineering Department, Middle East Technical University** by,

Prof. Dr. Halil Kalıpçılar
Dean, Graduate School of **Natural and Applied Sciences** _____

Prof. Dr. İlkay Ulusoy
Head of Department, **Electrical and Electronics Eng.** _____

Prof. Dr. S. Sencer Koç
Supervisor, **Electrical and Electronics Eng., METU** _____

Examining Committee Members:

Prof. Dr. Gülbin Dural
Electrical and Electronics Eng. Dept.,METU _____

Prof. Dr. S. Sencer Koç
Electrical and Electronics Eng., METU _____

Prof. Dr. Özlem Aydın Çivi
Electrical and Electronics Eng. Dept.,METU _____

Assoc. Prof. Dr. Lale Alatan
Electrical and Electronics Eng. Dept.,METU _____

Prof. Dr. Vakur B. Ertürk
Electrical and Electronics Eng. Dept.,Bilkent University _____

Date: 09.09.2019

I hereby declare that all information in this document has been obtained and presented in accordance with academic rules and ethical conduct. I also declare that, as required by these rules and conduct, I have fully cited and referenced all material and results that are not original to this work.

Name, Surname: Hülya Korkmaz

Signature:

ABSTRACT

DERIVATION AND ANALYSIS OF NEAR FIELD TO FAR FIELD TRANSFORMATION ALGORITHM FOR SPHERICAL SCANNING

Korkmaz, Hülya
Master of Science, Electrical and Electronics Engineering
Supervisor: Prof. Dr. S. Sencer Koç

September 2019, 88 pages

This thesis focuses on the improvement of a far field transformation algorithm of spherical near field scanning by using different quadrature techniques for numerical integration process. In this thesis, spherical vector wave expansion of **E** field is studied and numerical calculation for expansion coefficients of **E** field is performed. In the scope of this study quadrature techniques like Gauss, Trapezoid and Simpsons are investigated and advantages and disadvantages of these techniques are discussed. A decision criteria of quadrature technique for a particular function is also discussed and efficiency of these techniques is compared.

Spherical far field transformation algorithm considered in this study is applied to electric and magnetic Hertzian dipoles (directed on z axis and located at $(0,0,0)$) and expansion coefficients are calculated with Gauss, Trapezoid and Simpsons quadrature.

Also, expansion coefficients of Hertzian dipoles directed along the x axis and shifted along the z axis are calculated by using coordinate transformation and rotation. After the calculations of expansion coefficients, far field transformation is performed by using derived algorithm and far field radiations are plotted.

This study is mainly devoted on the far field transformation of a spherically scanned near field data and transformation of this data is performed by applying near field to far field transformation algorithm with Trapezoid and Simpsons quadrature techniques and effectiveness of these two techniques is discussed.

This study also includes the derivation of probe compensation algorithm to eliminate the probe effects from transformed data. In chapter 5, probe compensated coefficients are calculated by considering the coefficients of the probe and using the coordinate transformation and rotation. (See Appendix A and Appendix B). Far field pattern by using compensated coefficients is also analyzed to visualize the probe compensation effect.

Keywords: Vector Wave Expansion, Expansion Coefficients, Spherical Harmonics, Quadrature Techniques, Coordinate Transformation, Bessel Functions, Hankel Functions, Probe Compensation

ÖZ

KÜRESEL YAKIN ALAN ÖLÇÜMÜNÜ UZAK ALANA ÇEVİREN BİR ALGORİTMA GELİŞTİRİLMESİ VE ANALİZİ

Korkmaz, Hülya
Yüksek Lisans, Elektrik ve Elektronik Mühendisliği
Tez Danışmanı: Prof. Dr. S. Sencer Koç

Eylül 2019, 88 sayfa

Bu tez, küresel yakın alan ölçümünün değişik nümerik integral (quadrature) yöntemleri kullanılarak uzak alan çevirimini yapan bir algoritmanın incelenmesi üzerine yoğunlaşmaktadır. Bu çalışmada elektik alanın küresel vektör dalga açılımı (spherical vector wave expansion) incelenmekte ve bu açılım katsayıları için nümerik hesaplamalar gerçekleştirilmektedir. Çalışma kapsamında, Gauss, Trapezoid ve Simpson gibi nümerik integral yöntemleri araştırılmış ve bu yöntemlerin avantaj ve dezavantajları tartışılmıştır. Belirli bir fonksiyon için uygun nümerik integral tekniği belirleme kriterleri de tartışılmış ve bu tekniklerin etkinliği karşılaştırılmıştır.

Bu çalışmada dikkate alınan uzak alan çevirim algoritması elektrik ve manyetik dipol antenlere $(x, y, z = 0,0,0)$ noktasına yerleştirilmiş z yönlü) uygulanmış ve Gauss, Trapezoid ve Simpson teknikleri kullanılarak açılım katsayıları hesaplanmıştır.

Ayrıca, x yönlü Hertzian dipol ile ve z ekseninde kaydırılmış Hertzian dipolün açılım katsayıları koordinat dönüşümleri kullanılarak hesaplanmıştır. Açılım katsayılarının hesaplanmasının ardından geliştirilen algoritma kullanılarak Hertzian dipolün uzak alan dönüşümü gerçekleştirmiş ve uzak alan yayılım örüntüleri çizdirilmiştir.

Bu tez temel olarak küresel yakın alanda alınan anten ölçüm verisinin uzak alan çevrimine adanmıştır ve bu ölçüm verisinin uzak alan çevrimi Trapezoid ve Simpson teknikleri kullanılarak yapılmış ve bu iki tekniğin etkinliği tartışılmıştır.

Bu tez ayrıca, uzak alan çevrimi yapılan veriden prob etkisini gidermek için bir algoritma geliştirme çalışmasını da içermektedir. Prob açılım katsayıları ve koordinat dönüşümleri (Bknz: Ek A ve Ek B) kullanılarak, prob etkisi giderilmiş açılım katsayıları Bölüm 5'te hesaplanmış ve prob etkisini görebilmek için her iki durum için de uzak alan yaylım örüntüleri çizdirilmiştir.

Anahtar Kelimeler: Küresel Vektör Dalga Açılımı, Açılım Katsayıları, Vektörel Harmonikler, Nümerik İntegral Yöntemleri, Koordinat Dönüşümü, Bessel Fonksiyonları, Hankel Fonksiyonları, Prob Kompansasyonu

To my parents

ACKNOWLEDGEMENTS

I would like to express my sincere gratitude to my supervisor Prof. Dr. S. Sencer Koç for his patient guidance, encouragement and excellent technical suggestions throughout this study.

I would also like to thank Prof. Dr. Gülbin Dural, Prof. Dr. Özlem Aydın Çivi, Doç. Dr. Lale Alatan and Prof. Dr. Vakur B. Ertürk for their valuable participation to my jury.

I would also like to thank my friends Dr. Fatma Çalışkan, Ufuk Yıldız, Caner Bayram, Uğur Zöngür, Semih Alparslan, S. Hande Koru Başoğlu, H. Barkın Evgin, Orhan Atay, Tuba Düzel and Berna Pekavcılar for their valuable friendship, motivation and help throughout this study.

And finally, I am grateful to my family especially my mother Semiha KORKMAZ and my father Mürsel KORKMAZ for their endless love, support and encouragement during all my life.

TABLE OF CONTENTS

LIST OF TABLES

TABLES

LIST OF FIGURES

FIGURES

CHAPTER 1

INTRODUCTION

1.1 Scope of Thesis

Accurate measurement of the radiation pattern is an important task for both in design and implementation steps of an antenna. Antenna measurement necessitates the plane wave illumination of AUT (Antenna Under Test) which means that the distance between AUT and the probe antenna should be larger than $2D^2/\lambda$, where D is the maximum dimension of AUT and λ is the wavelength. This distance ($2D^2/\lambda$) is called as Rayleigh distance and generally accepted to define the far field of aperture type antennas [9]. Rayleigh distance ($2D^2/\lambda$) does not satisfy the far field conditions for all type of antennas, it is generally preferred for the antennas with a maximum dimension of $D \gg \lambda$.

Although Rayleigh distance is a basic requirement for an antenna measurement, constructing the far field conditions can be infeasible both in indoor and outdoor conditions for the antennas whose Rayleigh distance is in the order of meters. This restriction leads to indoor near field measurements where precision test range can be constructed in an anechoic chamber. This near field measurement needs a far field transformation due to the fact that antenna radiation pattern is defined in the far field.

The primary objective of this thesis is to construct a near field to far field transformation algorithm for spherical scanning which will be used as a transformation tool for an experimental spherical near field data. After the verification steps, updating the algorithm with the probe compensation ability is the second concentration of this thesis. In addition, different quadrature rules are studied in the development process of transformation algorithm and efficiencies of these techniques are compared.

This study starts with literature search to understand the theoretical basis, improvement of near field antenna measurement and far field transformation of this near field measurement. Near field to far field transformation for spherical scanning is studied by several authors. Frank Jensen [4] developed the theoretical background of near field measurement and far field transformation. Flemming Holm Larsen improved and extended these studies. A detailed exposition of the mathematical foundations of the far field transformation may be found in the book of Hansen [1] which is the main reference guide of this thesis. In literature, there are lots of articles about the near field antenna measurement and its far field transformation [4], [11], [16], [17], [19], [24]. In [11], J.E. Hansen and F. Jensen present their theoretical and experimental studies. Also study of Paris, Leach and Joy [28] summarizes the basic theory of probe compensated near field measurements. Wittmann and Stubenrauch [2] and Wacker [12] study on both theoretical and experimental issues of near field scanning.

1.2 Organization of Thesis

Chapter 1 summarizes the scope and organization of the thesis. In Chapter 2, basic concept of antenna radiation field regions is introduced, near field measurement techniques and their scanning types are examined. Planar, cylindrical and spherical near field measurements are detailed with their advantages and disadvantages. Also, brief history of the near field measurement is mentioned. And finally, comparison of scanning types is added to help choosing the best near field measurement technique for a particular antenna.

Chapter 3 focuses on the far field transformation algorithm of spherical near field measurement which is the main concern of this study. Mathematical background of solution of Helmholtz equation in spherical coordinates which is called “spherical vector wave function” is summarized and derivation of explicit expression of expansion coefficients is presented. For the numerical solution of expansion coefficients, quadrature techniques which can be applied to the derived integral are

studied. Quadrature techniques are examined and applied to plane wave and Hertzian dipole to determine their expansion coefficients and far field radiation patterns. Quadrature results are compared with the analytical values to decide which quadrature technique fits best for a given problem. Also, derived algorithm is applied to Hertzian dipole antennas which are directed on x axis and shifted along the z axis to ensure in the validity of the simulation code.

Chapter 4 is devoted on the far field transformation of spherically scanned near field data which is obtained by measurements in METU anechoic chamber. An experimental data is processed with derived algorithm by applying different quadrature techniques and efficiency of these techniques is compared. Far field radiation pattern of this experimental data is analyzed with Trapezoid and Simpson quadrature rules for different truncation order of N.

Chapter 5 includes the mathematical derivations and simulations for probe compensation. Far field transformation algorithm used in Chapter 4 is updated to eliminate the probe effect by implementing the mathematical derivations stated in Chapter 5. This new algorithm is applied to same experimental data in Chapter 4 and far field results with and without probe compensation are reported to compare the probe compensation effect.

Finally, Chapter 6 is a conclusion part which summaries the basic achievement acquired during this thesis.

CHAPTER 2

BASICS OF NEAR FIELD ANTENNA MEASUREMENT

An antenna is an essential component of radar, EW and telecommunication systems which receives and transmits the electromagnetic energy. Due to its important mission, designing an antenna is a challenging task for the designers from different branches and measurement of some antenna parameters such as gain, polarization and pattern is needed during antenna design cycle to characterize the antenna and compare the simulation results with experimental ones.

This measurement can be done both in the near field and the far field of an antenna which are shown in Figure 2-1 with the separation of reactive near field, radiating near field and far field.

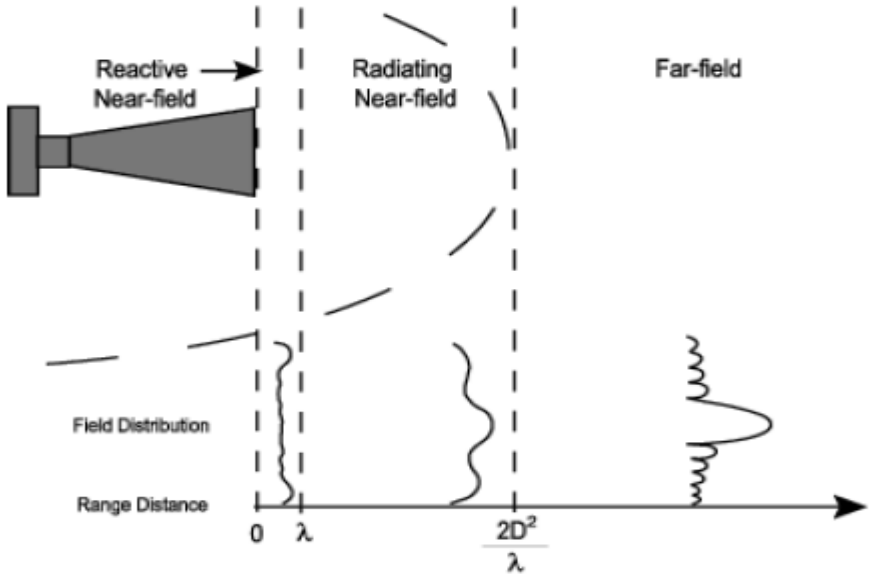

Figure 2-1: Propagating regions of an antenna [19]

Distance starting from $2D^2/\lambda$ to infinity is called the far field of an antenna where D is the maximum physical dimension of antenna and λ is the wavelength. In the far field region of antenna electric and magnetic fields decrease with a rate of $1/r$ where r is the distance from the antenna, but angular variation of a field does not depend on the distance r. [20]

The distance from antenna to far field distance is called as near field of an antenna and in this region radial and angular variation of electric and magnetic field depends on the distance. [20]

For the large antennas whose far field range extends the laboratory scales, making measurements in the near field and then obtaining the far field transformation is necessary and scientists have performed some studies on these topics.

2.1 Brief History

Following part is based on the study presented in [20]

"First near field antenna scanner "automatic antenna wave front plotter" was built by Barret and Barnes around 1950. They have performed all amplitude and phase measurements to fully characterize the pattern, but didn't perform far field transformation of near field measurement data. Five years later Richmond and Tice transformed the near field data to far field pattern and compared the results with the direct far field measurement and they obtained good agreement over the main beam and first few sidelobes. First probe corrected theories were studied between 1961-1975 and these theories were put into practice between 1965-1975. The first full three-dimensional plane wave solution with probe correction was performed by Kern in 1963. In 1965 first probe corrected near field measurement was performed at National Bureau of Standards using a plane scanning. Since near field antenna techniques requires numerical processing, it requires a high qualified computer, so with the improvement of computer processing capacity numerical calculations of near field techniques have improved in recent years. Higher frequency measurements, larger

scanners and spherical near field measurement theory is mostly studied subjects as a result of these improvements".

2.2 Near Field Scanning Types

Near field measurement is generally performed by using a network analyzer, computer, necessary RF components (such as amplifier) and the probe antenna which moves around the test antenna over a planar, cylindrical or spherical surface. A typical near field measurement setup is given in Figure 2-2.

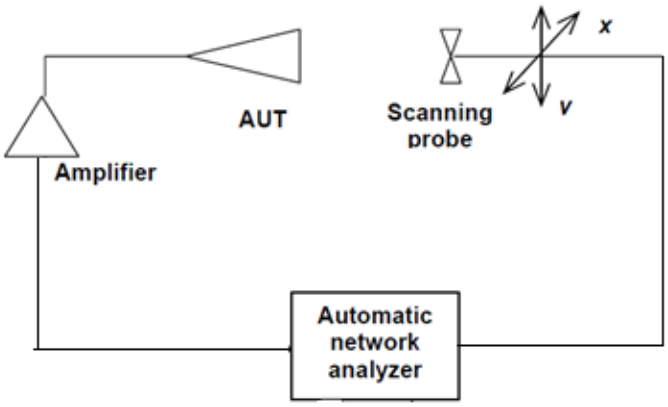

Figure 2-2: Typical near field antenna measurement

Near field measurement can be performed in three different scanning types as planar, cylindrical and spherical. For planar near field measurement, probe antenna is moved over a planar surface around a stationary test antenna both in X and Y directions as shown Figure 2-3.

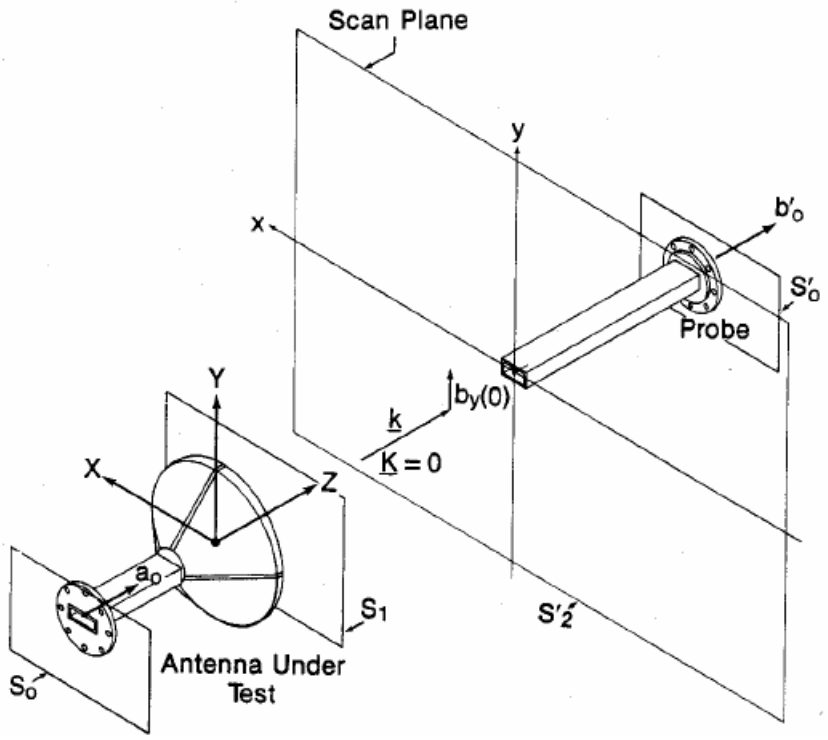

Figure 2-3: Planar near field antenna measurement setup [18]

Planar scanning is the simplest technique from the perspective of implementation and data processing algorithm compared with other scanning techniques. Planar is a convenient scanning technique for the large scale antennas such as an aircraft and high directive antennas.

For cylindrical near field measurement, probe antenna is moved over a cylindrical surface around a stationary test antenna as shown in Figure 2-4.

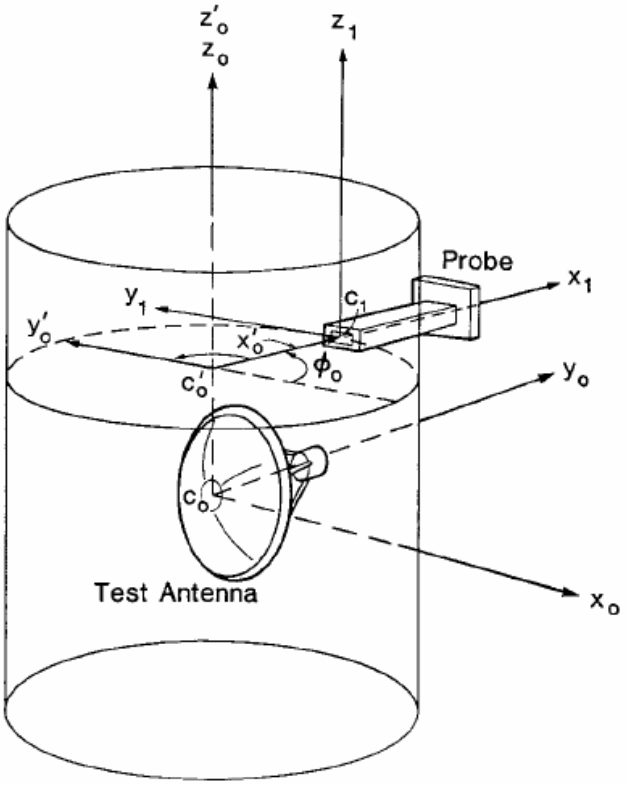

Figure 2-4: Cylindrical near field antenna measurement setup [18]

Cylindrical scanning is generally preferred for antennas which have omnidirectional radiation pattern in one plane.

In spherical near field measurement, test antenna is located at the center of a sphere and near field probe is moved along the sphere surface as shown in Figure 2-5.

Spherical scanning;

- Applicable to most type of antennas and all types of beams such as narrow, broad and omni,
- Compatible with an implementation of stationary probe and rotating test antenna,
- Requires more complicated data processing algorithm.

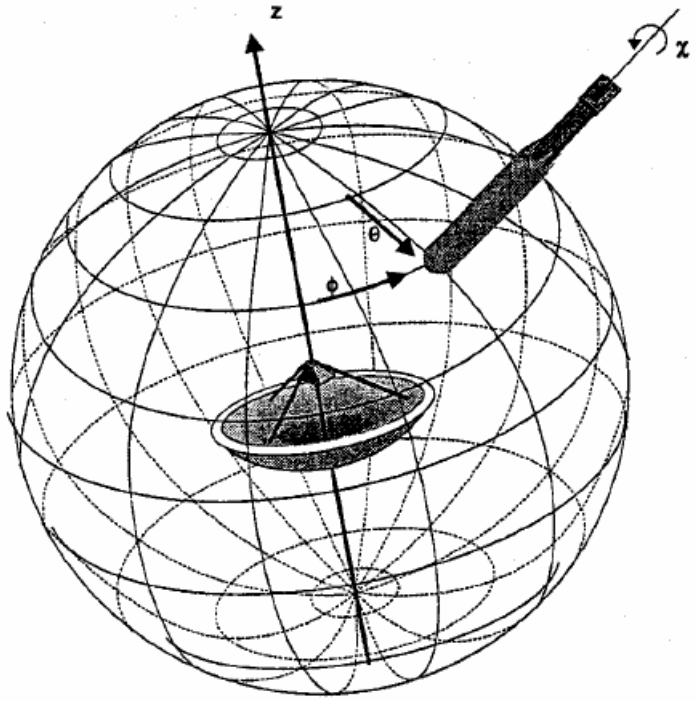

Figure 2-5: Spherical near field antenna measurement setup [18]

Table 2-1 compares the three scanning types based on some typical antenna characteristics.

Table 2-1: Comparison of near field antenna measurement types

Antenna Type / Parameter	**Planar**	**Cylindrical**	**Spherical**
High gain antennas	Excellent	Good	Good
Low gain antennas	Poor	Good	Excellent
Stationary AUT	Yes	Possible	Possible
Zero gravity simulation	Excellent	Poor	Variable
Alignment ease	Simple	Difficult	Difficult
Speed	Fast	Medium	Slow

CHAPTER 3

DERIVATIONS OF NEAR FIELD TO FAR FIELD TRANSFORMATION

3.1 Spherical Vector Wave Expansion

In a source free, linear, homogenous and isotropic region Maxwell equations state that both $\boldsymbol{E}$ and $\boldsymbol{H}$ fields satisfy the equation which is called as vector wave equation, or the Helmholtz equation [5] given in equation (3.1).

$$\nabla^2 \boldsymbol{E} + k^2 \boldsymbol{E} = 0 \tag{3.1}$$

$$k = \omega \sqrt{\mu\epsilon} \tag{3.2}$$

where k is propagation constant, ω is angular frequency, ϵ is the permittivity and μ is the permeability of the medium. The solutions of vector wave equation are called vector wave functions and they can be obtained by applying separation of variables in rectangular, cylindrical or spherical coordinate systems.

Since the spherical near field measurement analysis is the main concern of this thesis, spherical vector wave function solution will be detailed in this chapter.

In electromagnetic theory most of the problems are modeled and solved by using the spherical coordinate system shown in Figure 3-1.

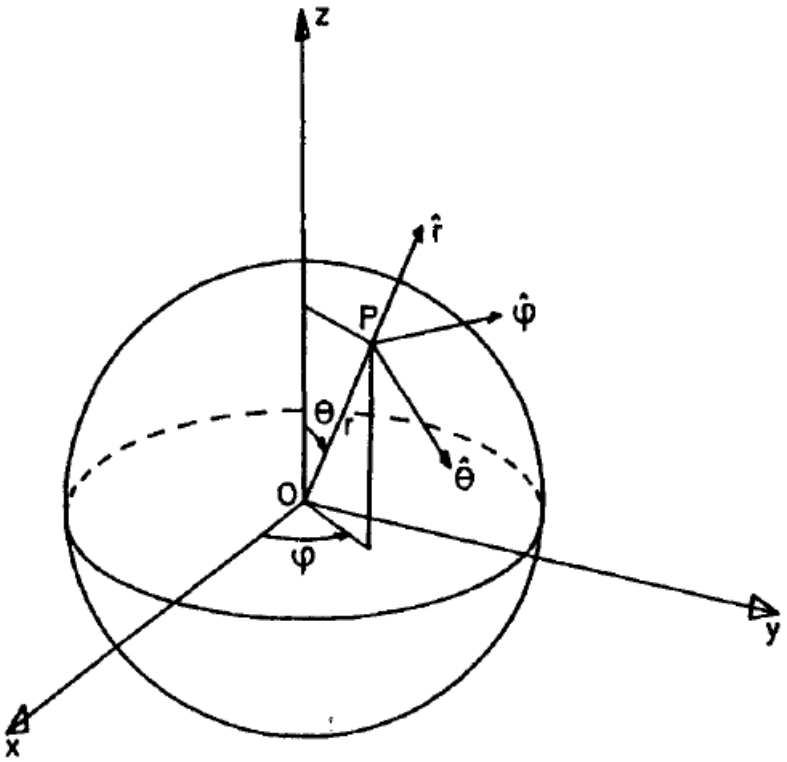

Figure 3-1: Spherical coordinate system and unit vectors [1]

An electric field can be represented in the spherical coordinate system as:

$$\boldsymbol{E}(r,\theta,\phi) = E_r(r,\theta,\phi)\boldsymbol{a}_r + E_\theta(r,\theta,\phi)\boldsymbol{a}_\theta + E_\phi(r,\theta,\phi)\boldsymbol{a}_\phi \qquad (3.3)$$

Let $\psi(r,\theta,\phi)$ be a scalar function that can represent a field or vector protentional component and satisfies the scalar wave equation, $\nabla^2\psi + k^2\psi = 0$. Solution of this equation by using separation of variables in spherical coordinates as in the form;

$$\psi(r,\theta,\phi) = z_n^{(a)}(kr)P_n^m(\cos\theta)e^{jm\phi} \qquad (3.4)$$

where $e^{jm\phi}$ states the ϕ dependency, $P_n^m(\cos\theta)$ is the associated Legendre function states the θ dependency and $z_n^{(a)}$ states one of the following functions according to the upper index a with a time convention of $e^{j\omega t}$.

$$z_n^{(1)} = j_n(kr) \quad \text{Spherical Bessel Function} \tag{3.5}$$

$$z_n^{(2)} = y_n(kr) \quad \text{Spherical Neumann Function} \tag{3.6}$$

$$z_n^{(3)} = h_n^{(1)}(kr) \quad \text{Spherical Hankel Function Type 1} \tag{3.7}$$

$$z_n^{(4)} = h_n^{(2)}(kr) \quad \text{Spherical Hankel Function Type 2} \tag{3.8}$$

$a = 1$ and $a = 2$ are used for standing waves, $a = 3$ is used for inward travelling wave and $a = 4$ is used for outward travelling wave, as summarized in Table 3-1.

Table 3-1: $z_n^{(a)}$ Function types based on wave characteristics [5]

Wave Type	**Wave Functions**	**Zeros of Wave Functions**	**Infinities of Wave Functions**
Traveling waves	$h_n^{(1)}(kr) = j_n(kr) + jy_n(kr)$ for $-r$ travel	$kr \rightarrow +j\infty$	$kr = 0$ $kr \rightarrow -j\infty$
	$h_n^{(2)}(kr) = j_n(kr) - jy_n(kr)$ for $+r$ travel	$kr \rightarrow -j\infty$	$kr = 0$ $kr \rightarrow +j\infty$
Standing waves	$j_n(kr)$ for $\pm r$	Infinite number	$kr \rightarrow \pm j\infty$
	$y_n(kr)$ for $\pm r$	Infinite number	$kr = 0$ $kr \rightarrow \pm j\infty$

Spherical form of Bessel and Hankel functions stated in equations 3.9, 3.10 and 3.11 are considered throughout this study.

For spherical standing wave,

$$j_n(z) = \sqrt{\frac{\pi}{2z}}\, J_{n+\frac{1}{2}}(z)\,, \tag{3.9}$$

For inward spherical travelling wave,

$$h_n^{(1)}(z) = \sqrt{\frac{\pi}{2z}}\, H^{(1)}_{n+\frac{1}{2}}(z)\,, \tag{3.10}$$

For outward spherical travelling wave,

$$h_n^{(2)}(z) = \sqrt{\frac{\pi}{2z}}\, H^{(2)}_{n+\frac{1}{2}}(z)\,. \tag{3.11}$$

In addition to the spherical form of Bessel and Hankel functions, asymptotic form of spherical Bessel and Hankel functions (3.12, 3.13, 3.14 and 3.15) must be taken into consideration for the far field calculations.

$$\lim_{x\to\infty} j_n^{(1)} = \frac{1}{x}\cos\left(x - (n+1)\frac{\pi}{2}\right) \tag{3.12}$$

$$\lim_{x\to\infty} y_n^{(1)} = \frac{1}{x}\sin\left(x - (n+1)\frac{\pi}{2}\right) \tag{3.13}$$

$$\lim_{x\to\infty} h_n^{(1)} = (-i)^{n+1}\frac{e^{ix}}{x} \tag{3.14}$$

$$\lim_{x\to\infty} h_n^{(2)} = (i)^{n+1}\frac{e^{-ix}}{x} \tag{3.15}$$

3.1.1 Products of Spherical Harmonics

Spherical harmonic, Y_{nm} notation stated by Jackson [29] is,

$$Y_{nm}(\theta,\phi) = D_{nm} P_n^m(\cos\theta) e^{jm\phi} \tag{3.16}$$

where P_n^m is a Legendre function defined by,

$$P_n^m(x) = \frac{(-1)^m}{2^n n!}(1-x^2)^{m/2}\frac{d^{n+m}(x^2-1)^n}{dx^{n+m}} \tag{3.17}$$

$$P_n^{-m}(x) = (-1)^m \frac{(n-m)!}{(n+m)!} P_n^m(x) \tag{3.18}$$

and D_{nm} is defined as,

$$D_{nm} = \sqrt{\frac{2n+1}{4\pi}\frac{(n-m)!}{(n+m)!}} \tag{3.19}$$

From equations (3.17), (3.18) and (3.19) it can be derived as,

$$Y_{n,-m}(\theta,\phi) = (-1)^m\, Y_{n,m}^* \tag{3.20}$$

Spherical harmonics, $Y_{nm}(\theta,\phi)$ are orthogonal over a spherical surface.

$$\int_0^{\pi}\int_0^{2\pi} Y_{nm}(\theta,\phi)\, Y_{\nu\mu}^* \sin\theta\, d\phi\, d\theta = \delta_{n\nu}\delta_{m\mu} \tag{3.21}$$

$$\delta_{n\nu} = \begin{cases} 1, & n = \nu \\ 0, & n \neq \nu \end{cases} \tag{3.22}$$

$$\delta_{m\mu} = \begin{cases} 1, & m = \mu \\ 0, & m \neq \mu \end{cases} \tag{3.23}$$

$\varphi_{nm}^{(a)}(k,\boldsymbol{r})$ can be defined as,

$$\varphi_{nm}^{(a)}(k,\boldsymbol{r}) = z_n^{(a)}(kr)Y_{nm}(\hat{\boldsymbol{r}}) \tag{3.24}$$

where $z_n^{(a)}(kr)$ can be chosen from the functions given in the equations (3.9), (3.10) and (3.11) according to the upper index a, and $\hat{\boldsymbol{r}}$ is used as a shorthand notation for the two angular variables (θ,ϕ).

3.1.2 Explicit Formulas of Expansion Coefficients

In a source free region, the multipole expansion of an electric field can be written as [23];

$$\boldsymbol{E}(\boldsymbol{r}) = \sum_{n=0}^{\infty}\sum_{m=-n}^{n} a_{nm}\boldsymbol{M}_{nm}^{(a)}(k,\boldsymbol{r}) + b_{nm}\boldsymbol{N}_{nm}^{(a)}(k,\boldsymbol{r}) \tag{3.25}$$

and the multipole expansion of the corresponding magnetic field can be written as [23];

$$\boldsymbol{H}(\boldsymbol{r}) = jY\sum_{n=0}^{\infty}\sum_{m=-n}^{n} b_{nm}\boldsymbol{M}_{nm}^{(a)}(k,\boldsymbol{r}) + a_{nm}\boldsymbol{N}_{nm}^{(a)}(k,\boldsymbol{r}) \tag{3.26}$$

where $Y = \sqrt{\epsilon/\mu}$ is the medium admittance

$\boldsymbol{M}_{nm}^{(a)}(k,\boldsymbol{r})$ and $\boldsymbol{N}_{nm}^{(a)}(k,\boldsymbol{r})$ can be derived as follows [23];

$$\boldsymbol{M}_{nm}^{(a)}(k,\boldsymbol{r}) = \nabla \times \boldsymbol{r}\varphi_{nm}^{(a)}(k,\boldsymbol{r}) \tag{3.27}$$

$$\boldsymbol{M}_{nm}^{(a)}(k,\boldsymbol{r}) = z_n^{(a)}(kr)\left[\frac{jm}{\sin\theta}Y_{nm}(\theta,\phi)\boldsymbol{a}_\theta - \frac{\partial Y_{nm}(\theta,\phi)}{\partial\theta}\boldsymbol{a}_\phi\right] \tag{3.28}$$

$$\left(\boldsymbol{M}_{nm}^{(a)}\right)^{*} = \boldsymbol{M}_{n,-m}^{(a)} \tag{3.29}$$

$$\boldsymbol{N}_{nm}^{(a)}(k,\boldsymbol{r}) = \frac{1}{k}\nabla \times \boldsymbol{M}_{nm}^{(a)}(k,\boldsymbol{r}) \tag{3.30}$$

$$\begin{aligned}\boldsymbol{N}_{nm}^{(a)}(k,\boldsymbol{r}) = {} & \frac{z_n^{(a)}(kr)}{kr} n(n+1) Y_{nm}(\theta,\phi)\boldsymbol{a}_r \\ & + \frac{1}{kr}\frac{d\left(rz_n^{(a)}(kr)\right)}{dr}\left[\frac{\partial Y_{nm}(\theta,\phi)}{\partial\theta}\boldsymbol{a}_\theta + \frac{jm}{\sin\theta} Y_{nm}(\theta,\phi)\boldsymbol{a}_\phi\right]\end{aligned} \tag{3.31}$$

$$\left(\boldsymbol{N}_{nm}^{(a)}\right)^{*} = \boldsymbol{N}_{n,-m}^{(a)} \tag{3.32}$$

Far field transformation algorithm is based on calculating the multipole expansion coefficients, a_{nm} and b_{nm} in the equations (3.25) and (3.26). Explicit expressions for these coefficients are needed for numerical calculations and steps specified below can be followed to get the explicit expressions.

1. Multiply both side of equation (3.25) with $\left(\boldsymbol{M}_{\nu\mu}^{(a)}(k,\boldsymbol{r})\right)^{*}$ and integrate over a sphere, it must be pointed out that conjugation is not applied on the radial functions.

$$\int_0^{2\pi}\int_0^{\pi} \boldsymbol{E}(\boldsymbol{r}).\left(\boldsymbol{M}_{\nu\mu}^{(a)}(k,\boldsymbol{r})\right)^{*} \sin\theta\, d\theta\, d\phi = \tag{3.33}$$

$$\int_0^{2\pi}\int_0^{\pi}\left(\sum_{n=0}^{\infty}\sum_{m=-n}^{n} a_{nm}\boldsymbol{M}_{nm}^{(a)}(k,\boldsymbol{r}) + b_{nm}\boldsymbol{N}_{nm}^{(a)}(k,\boldsymbol{r})\right).\left(\boldsymbol{M}_{\nu\mu}^{(a)}(k,\boldsymbol{r})\right)^{*}\sin\theta\, d\theta\, d\phi$$

2. Use the orthogonality properties of the vector wave functions given in equation (3.34) which eliminates the term with b_{nm}. After some manipulation, explicit expression for a_{nm} is obtained as in equation (3.37).

$$\int_0^{2\pi}\int_0^{\pi} \boldsymbol{N}_{nm}^{(a)}(k,\boldsymbol{r}).\left(\boldsymbol{M}_{\nu\mu}^{(b)}(k,\boldsymbol{r})\right)\sin\theta\, d\theta\, d\phi = 0 \tag{3.34}$$

$$\int_0^{\pi} P_\nu^m P_n^m \sin\theta\, d\theta = \frac{2}{2n+1}\frac{(n-m)!}{(n+m)!}\delta_{\nu n} \tag{3.35}$$

$$\int_0^{\pi}\left[\frac{dP_\nu^m}{d\theta}\frac{dP_n^m}{d\theta} + \frac{m^2 P_\nu^m P_n^m}{(\sin\theta)^2}\sin\theta\, d\theta\right] = \frac{2}{2n+1}\frac{(n-m)!}{(n+m)!}n(n+1)\delta_{\nu n} \tag{3.36}$$

$$a_{nm} = \frac{1}{\nu(\nu+1)(z_\nu^a)^2(kr)\delta_{n\nu}\delta_{m\mu}}\int_0^{2\pi}\int_0^{\pi}\boldsymbol{E}(\boldsymbol{r}).\left(\boldsymbol{M}_{\nu\mu}^{(a)}(k,\boldsymbol{r})\right)^*\sin\theta\, d\theta\, d\phi \tag{3.37}$$

3. Same mathematical procedure can be applied for explicit expression of b_{nm}. Multiply both side of equation (3.25) by $\left(\boldsymbol{N}_{\nu\mu}^{(a)}(k,\boldsymbol{r})\right)^*$ and integrate over a unit sphere as in equation (3.38). Again, it must be remembered that conjugation is not applied on the radial functions.

$$\begin{aligned}&\int_0^{2\pi}\int_0^{\pi}\boldsymbol{E}(\boldsymbol{r})\cdot\left(\boldsymbol{N}_{\nu\mu}^{(a)}(k,\boldsymbol{r})\right)^*\sin\theta\, d\theta d\phi \\ =&\int_0^{2\pi}\int_0^{\pi}\left(\sum_{n=0}^{\infty}\sum_{m=-n}^{n} a_{nm}\boldsymbol{M}_{nm}^{(a)}(k,\boldsymbol{r}) + b_{nm}\boldsymbol{N}_{nm}^{(a)}(k,\boldsymbol{r})\right).\left(\boldsymbol{N}_{\nu\mu}^{(a)}(k,\boldsymbol{r})\right)^*\sin\theta\, d\theta d\phi\end{aligned} \tag{3.38}$$

4. Equation (3.34) directly eliminates the term with a_{nm} and by using equation (3.39) explicit expression for b_{nm} can be easily derived as,

$$\int_0^{2\pi}\int_0^{\pi} \boldsymbol{N}_{nm}^{(a)}(k,\boldsymbol{r})\left(\boldsymbol{N}_{\nu\mu}^{(a)}(k,\boldsymbol{r})\right)^{*}\sin\theta d\theta\, d\phi = \begin{bmatrix} \left(\nu(\nu+1)\dfrac{z_\nu^{(a)}(kr)}{kr}\right)^2 + \\ \nu(\nu+1)\left(\dfrac{1}{kr}\dfrac{d(rz_\nu^{(a)}(kr))}{dr}\right)^2 \end{bmatrix}\delta_{n\nu}\delta_{m\mu} \quad (3.39)$$

$$b_{nm} = \frac{\int_0^{2\pi}\int_0^{\pi}\boldsymbol{E}(\boldsymbol{r}).\left(\boldsymbol{N}_{\nu\mu}^{(a)}(k,\boldsymbol{r})\right)^{*}\sin\theta\, d\theta\, d\phi}{\left[\left(\nu(\nu+1)\dfrac{z_\nu^{(a)}(kr)}{kr}\right)^2 + \nu(\nu+1)\left(\dfrac{1}{kr}\dfrac{d\left(rz_\nu^{(a)}(kr)\right)}{dr}\right)^2\right]\delta_{n\nu}\delta_{m\mu}} \quad (3.40)$$

Equation 3.25 states that in a source free region $\boldsymbol{E}$ field can be written as a summation of multipole coefficients multiplied by vector wave functions $\boldsymbol{M}$ and $\boldsymbol{N}$ at any point of space both in near field and far field. Multipole coefficients given in the equations 3.37 and 3.40 can be used for the calculations of far field $\boldsymbol{E}$ with the asymptotic form of vector wave functions $\boldsymbol{M}$ and $\boldsymbol{N}$. The asymptotic form of vector wave functions can be calculated by using asymptotic form of appropriate spherical Bessel and Hankel functions given in equations 3.12, 3.13, 3.14 and 3.15. Far field $\boldsymbol{H}$ can also be calculated with same procedure. It can be concluded that near field to far field transformation algorithm is based on determining the multipole coefficients from near field $\boldsymbol{E}$ or $\boldsymbol{H}$ and evaluating the far field $\boldsymbol{E}$ or $\boldsymbol{H}$ by using these calculated coefficients and asymptotic form of vector wave functions.

3.2 Numerical Solution for Expansion Coefficients

Explicit formulas for a_{nm} and b_{nm} are derived as given in the equations (3.37) and (3.40) which include double integrals with the requirement of numerical calculations. Next step is to examine quadrature techniques for the numerical calculations of these double integrals.

3.2.1 Numerical Integration Theory

Definite integral of a function $f(x)$ can be evaluated by the area under $f(x)$ curve between the points $[a, b]$ as shown in Figure 3-2.

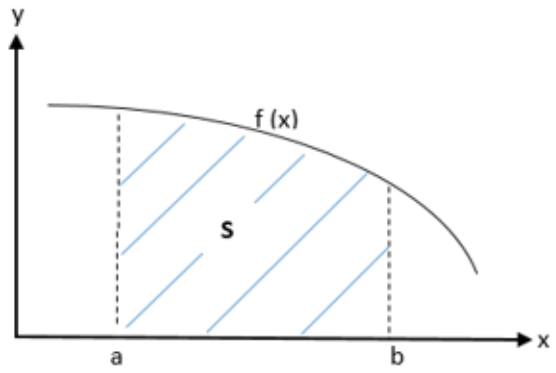

Figure 3-2: Definite integral of a function

Calculating the value of a definite integral with analytical methods is not feasible for the following cases:

- For an integrand without an antiderivative,
- Integration of an experimental data rather than known function,
- For a function requiring high analytical calculation load than numerical integration.

An alternative solution for the above cases is to use the numerical integration which is an approximate computation of an integral by using numerical integration technique, quadrature.

Basic approach of quadrature is to estimate the value of an integral by using weights A_i and values of function at x_i where choice of A_i and x_i depends on the quadrature technique to be used.

$$\int_a^b f(x) \rightarrow \sum_{i=1}^{n} A_i \, f(x_i) \tag{3.41}$$

3.2.2 Quadrature Techniques

Numerical integration techniques which are also called as quadrature can be classified into two main groups as Newton Cotes and Gauss quadrature techniques.

Newton Cotes formulas use equally spaced points for the evaluation of the numerical integration and they are based on the approach of replacing the function to be integrated by an approximate one which best fits with original and is easier to integrate. These formulas work best if the approximate function is smooth such as polynomial given in (3.42)

$$I = \int_a^b f(x)\, dx \quad \text{where } f(x) \approx f_n\,(x)$$
$$f_n\,(x) = a_0 + a_1 x + \cdots + a_{n-1} x^{n-1} + a_n x^n \tag{3.42}$$

Trapezoid rule, Midpoint rule and Simpson rule are common types of Newton Cotes formulas and details of these techniques are given in the following part.

Trapezoid rule converges the integral of $f(x)$ by evaluating the area of the trapezoid under the function $f(x)$ given in Figure 3-3 with the formula of (3.43).

$$S = \frac{f(b) + f(a)}{2}(b - a) \tag{3.43}$$

where S is the are of trapezoid under the curve of $f(x)$.

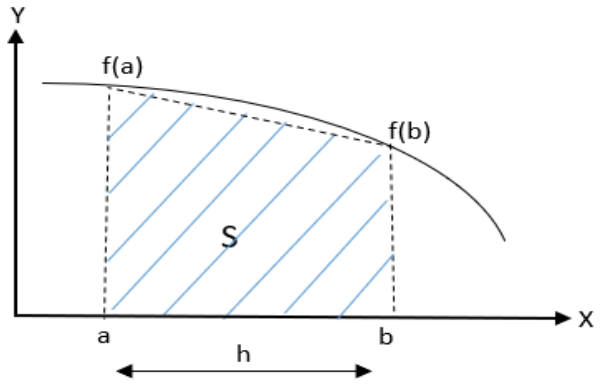

Figure 3-3: Trapezoid quadrature

The integration interval can be divided into smaller sub intervals and Trapezoid rule is applied to each sub interval separately as given in the equations (3.44) and (3.45) for better approximation of the integral and this is called as composite Trapezoid rule.

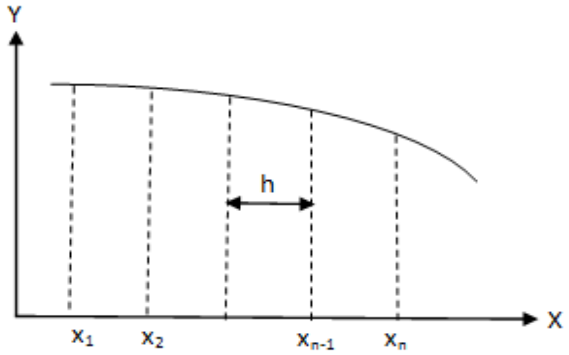

Figure 3-4: Composite Trapezoid quadrature

$$\int_{a}^{b} f(x)\,dx = \int_{a}^{a+h} f(x)\,dx + \int_{a+h}^{a+2h} f(x)\,dx + \cdots \int_{a+(n-1)h}^{b} f(x)\,dx \qquad (3.44)$$

$$\int_{a}^{b} f(x)\,dx = \frac{(b-a)}{2n}\left[f(a) + 2\left(\sum_{i=1}^{n-1} f(a+ih)\right) + f(b)\right] \qquad (3.45)$$

Since quadrature is an approximation technique, error between quadrature and definite value is inevitable, and this error for composite Trapezoid rule can be defined as:

$$E \leq \frac{5(b-a)^3}{12n^2} \max\left(|f''(x)|\right) \tag{3.46}$$

where E is the error caused by composite Trapezoid quadrature, $f''(x)$ is the second derivative of function f at some point x inside the interval $a \leq x \leq b$ and n is the number of sub intervals.

Other type of Newton Cotes formula is called as Midpoint rule which is based on calculation of a rectangular area created by the points $(a, 0)$, $(b, 0)$, $\left(a, f\left(\frac{a+b}{2}\right)\right)$ and $\left(b, f\left(\frac{a+b}{2}\right)\right)$ and the formula for this approximation is given in equation (3.47)

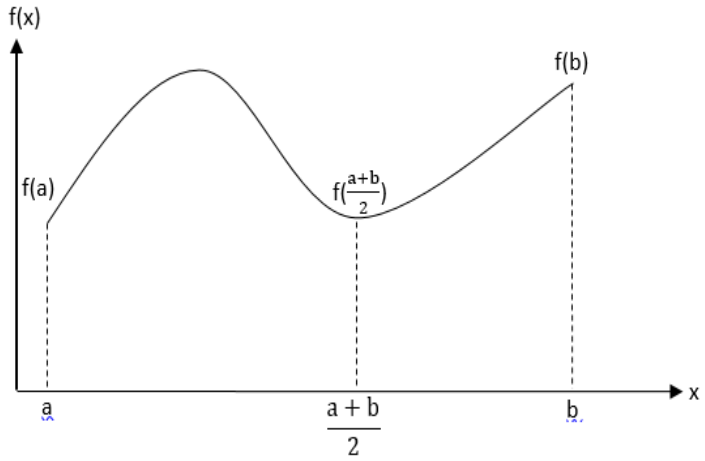

Figure 3-5: Midpoint quadrature

$$\int_a^b f(x)\,dx = (b-a) f\left(\frac{a+b}{2}\right) \tag{3.47}$$

The integration interval can be divided into smaller sub intervals and Midpoint rule is applied to each sub interval as given in the equations (3.48), (3.49), (3.50), and (3.51) and this is called as composite Midpoint rule.

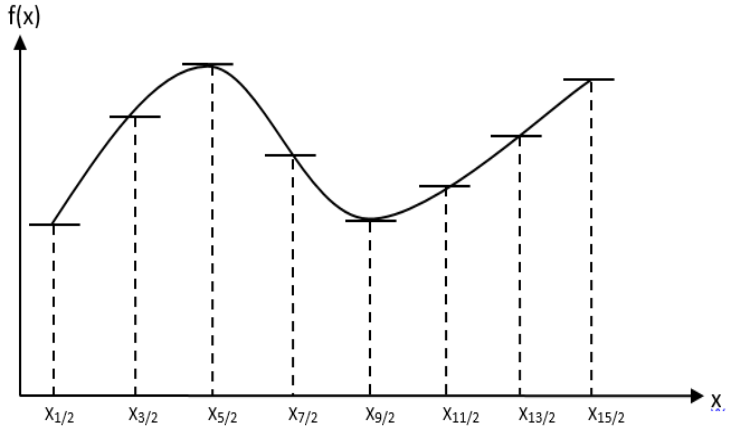

Figure 3-6: Composite Midpoint quadrature

$x_i = a + \left(i - \frac{1}{2}\right) h$ with $i = 1,2, \ldots n$

$$\int_a^b f(x)\,dx = h \sum_{i=1}^{n} f(x_i) = h \sum_{i=1}^{n} f\left(a + \left(i - \frac{1}{2}\right) h\right) \tag{3.48}$$

$$h = \frac{(b-a)}{n} \tag{3.49}$$

$$\int_a^b f(x)\,dx = \int_{x_0}^{x_2} f(x)\,dx + \int_{x_2}^{x_4} f(x)\,dx + \cdots + \int_{x_{n-4}}^{x_{n-2}} f(x)\,dx + \int_{x_{n-2}}^{x_n} f(x)\,dx \tag{3.50}$$

$$\int_a^b f(x)\,dx = \frac{(b-a)}{3n}\left[f(x_0) + 4\sum_{i=1}^{n-1} f(x_i) + 2\sum_{i=2}^{n-2} f(x_i) + f(x_n)\right] \tag{3.51}$$

The error of Midpoint quadrature technique is given in equation (3.52)

$$E \leq \frac{5(b-a)^3}{24n^2} \max\left(|f''(x)|\right) \tag{3.52}$$

where E is the error caused by composite Midpoint quadrature, $f''(x)$ is the second derivative of function $f$at some point x inside the interval $a \leq x \leq b$ and n is the number of sub intervals.

Simpson quadrature is another type of Newton Cotes formula which is based on the approximation of an integrand $f(x)$ with a second order polynomial $f_2(x)$ as given in equation (3.53)

$$\int_a^b f(x)\,dx \approx \int_a^b f_2(x)\,dx = \int_a^b a_0 + a_1 x + a_2 x^2 dx \tag{3.53}$$

$$f_2(x) = a_0 + a_1 x + a_2 x^2$$

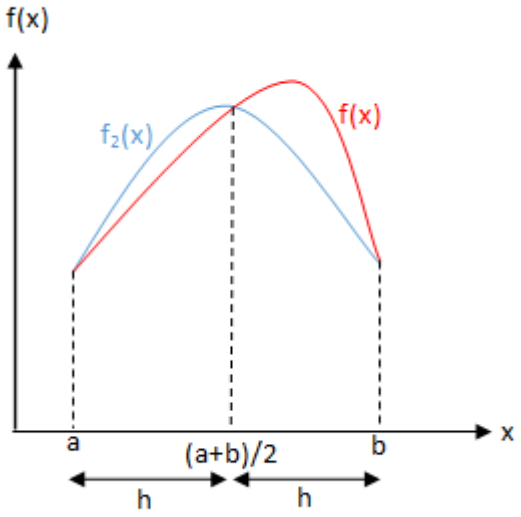

Figure 3-7: Simpson quadrature

One may use $(a, f(a))$, $(a+b)/2, f\ ((a+b)/2)$, $(b, f(b))$ to evaluate a_0, a_1, a_2 and $h = (b-a)/n$

$$\int_a^b f_2(x)\,dx = \frac{h}{3}\left[f(a) + 4f\left(\frac{a+b}{2}\right) + f(b)\right] \tag{3.54}$$

The integration interval can be divided into smaller sub intervals and Simpson rule is applied to each sub interval and this is called as composite Simpson rule. The error of Simpson quadrature technique is given as in equation (3.55)

$$E \leq \frac{5(b-a)^5}{180n^4} \max\left(|f''(x)|\right) \tag{3.55}$$

where E is the error caused by composite Simpson quadrature, $f''(x)$ is the second derivative of function f at some point x inside the interval $a \leq x \leq b$ and n is the number of sub intervals.

Quadrature techniques have been divided into two main groups as Newton Cotes and Gauss Quadrature rules. Newton Cotes formulas are detailed as Trapezoid, Midpoint and Simpson rules so far. Gauss quadrature determines the best fit integration points to achieve the most accurate result, rather than equally spaced points as in Newton-Cotes quadrature. Gauss quadrature is generally preferred in case of expensive evaluation of a function since it requires fewer calculations.

Gauss quadrature uses orthogonal polynomials over the interval $w(x)$, instead of using polynomial as in Newton Cotes formulas and this technique is based on representing the integrand as a product of $w(x)$ and polynomial $P(x)$ as in equation (3.56).

$$f(x) = w(x)P(x) \tag{3.56}$$

Then, numerical integration by Gauss quadrature is calculated with the multiplication of weighting factor and evaluated values of a function at the zeros of polynomial $P(x)$ as in (3.57).

$$\int_a^b f(x)\,dx \approx \sum_{i=1}^{n} w_i\, f(x_i) \tag{3.57}$$

List of the applicable Gauss quadrature techniques for a particular type of a function is presented in Table 3-2.

Table 3-2: Integral types and applied Gauss quadrature techniques

Integral Type	Applied Gauss Quadrature Type
$\int_a^b f(x)\,dx$	Gauss Legendre
$\int_{-\infty}^{\infty} e^{-x^2} f(x)\,dx$	Gauss Hermite
$\int_0^{\infty} e^{-x^2} f(x)\,dx$	Gauss Laguerre

(Table 3-2 continued)

$\int_{-1}^{1} \frac{1}{\sqrt{1-x^2}} f(x)\,dx$	Gauss Chebyshev I
$\int_{-1}^{1} \sqrt{1-x^2} f(x)\,dx$	Gauss Chebyshev II

3.2.3 Comparison of Quadrature Techniques

Quadrature is inevitable method for a scientific problem with an integral which cannot be evaluated analytically. Choosing the proper quadrature technique is an important step to result with a minimum error, time and calculation load. There is no best quadrature technique which works best for all type of functions, it depends on the properties of a function to be evaluated. The points specified below must be considered to achieve best result with minimum error:

- Newton Cotes methods should be applied for uniform data points and Gauss quadrature should be applied for nonuniform data points,
- Smoothness, singularities and their locations of an integrand should be determined and most appropriate quadrature technique must be chosen,
- Classical quadrature techniques such as Newton Cotes and Gauss don't work well with highly oscillatory integrands and some special techniques like the Filon method and Levin method studied by Krishna Thapa in [27] should be chosen for these integrands,
- Effectiveness is the ability of quadrature technique to be successful to achieve intended numerical results, so required accuracy and acceptable error should be determined before the calculation and the most effective quadrature technique must be chosen to fit predefined values,
- Redundant calculations (like increasing composite grid points) don't increase the accuracy and may result with a high computation load. Adjusting the calculation load to an optimal level can decrease the time

and budget requirements especially for the huge data whose processing requires high capacity computer and long time.

3.3 Numerical Results for Expansion Coefficients of Plane Wave and Hertzian Dipole

Explicit formulas for the multipole coefficients are derived and the quadrature techniques are studied for the numerical calculations of these coefficients so far. Next step covers application of studied quadrature techniques to multipole coefficients of plane wave and Hertzian dipole to verify the first part of an algorithm. In the scope of this section, different quadrature techniques will be used and results of these techniques will be compared with both each other and analytical values.

3.3.1 Expansion Coefficients for Plane Wave

Electric field expression for an x-polarized plane wave propagating in $+z$ direction is given as in equation (3.58).

$$\boldsymbol{E}(\mathrm{r}) = E_0 \boldsymbol{a_x} e^{-jkz} \tag{3.58}$$

The spherical harmonic expansion of this wave can be written as,

$$\boldsymbol{E}(\boldsymbol{r}) = \sum_{n,m} a_{nm} \boldsymbol{M}_{nm}^{(1)} + b_{nm} \boldsymbol{N}_{nm}^{(1)} \tag{3.59}$$

where we have dropped the arguments of the vector wave functions for notational simplicity. Since the plane wave does not have a singularity, only first type of spherical functions can be used in this expansion. Since an analytic expression for the field is available, the spherical harmonic coefficients can be obtained analytically as in [23],

$$a_{nm} = (-j)^{n-1} E_0 \sqrt{\frac{\pi(2n+1)}{n(n+1)}} \delta_{m,\pm 1} \tag{3.60}$$

$$b_{nm} = -m(-j)^{n-1}E_0\sqrt{\frac{\pi(2n+1)}{n(n+1)}}\delta_{m,\pm1} \tag{3.61}$$

Note that only the coefficients with $m = \pm 1$ exist because of the ϕ symmetry. For the evaluation of the spherical harmonic coefficients a_{nm} and b_{nm}, the expressions stated in equations (3.37) and (3.40) are used. The integrals in these equations are evaluated by using Gaussian, Trapezoid, Simpson quadrature rules and MATLAB® integral2 function which evaluates a double integral numerically with an adaptive quadrature technique. The coefficients thus obtained are also used to obtain the far field value of the field which should again be an x polarized plane wave propagating in $+z$ direction. Table 3-3 summarizes the results of the developed code with different quadrature techniques and for all quadrature techniques software gives zero output for the inputs where m is different from ± 1 as expected from analytical calculations. If the results of four different quadrature rules are compared, MATLAB® integral2 and Gaussian give similar results which are also same with the analytical values, but the results for Trapezoid and Simpson quadrature are a little bit different from other quadrature techniques although they have more grid points than Gaussian. Since Trapezoid and Simpson quadrature calculate the coefficients of given plane wave with more error compared the other techniques, it is recommended to apply integral2 and Gaussian quadrature for multipole coefficient calculations of a plane wave.

Next step after the calculation of multipole coefficients is to evaluate far field $\boldsymbol{E}$ and $\boldsymbol{H}$ given in equations (3.25) and (3.26) which state the range of n is zero to infinity, but in practice it is not possible to take infinitely many terms into account which obliges us to truncate the infinite series at some finite value N.

"The number of terms that must be kept in the summation, N depends on the value of kr as well as the desired accuracy. As r is increased, more terms are required to keep the accuracy at the desired level. On the other hand, if too many terms are used so that N is large, the spherical Hankel functions oscillate wildly with exponentially

large values, causing numerical inaccuracies. This occurs when the order exceeds the argument, hence the condition". [13]

Multipole coefficients of plane wave from software output for $E_0 = 1$, $kr = 10$, 20 θ, 25 ϕ grid points for Gauss rule, 315 θ, 629 ϕ grid points for Trapezoid and Simpson rules are listed in Table 3-3 which shows that error increases after n is bigger than $2kr$, 20. This result shows that truncation point for n should be in the order of $2kr$ for a minimum error factor and to avoid unnecessary calculation load.

Table 3-3: Coefficients for plane wave with different quadrature techniques

(n,m)	**Analytical Value**		**integral2**		**Gauss**		**Trapezoid**		**Simpson**	
	a_{nm}	b_{nm}	a_{nm}	b_{nm}	a_{nm}	b_{nm}	a_{nm}	b_{nm}	a_{nm}	b_{nm}
$(1,\pm1)$	2.1708	$\mp$2.1708	2.1708	$\mp$2.1708	2.1708	$\mp$2.1708	2.1705 + 0.0002i	$\mp$2.1304 $\mp$ 0.0001i	2.1656 + 0.0002i	$\mp$2.1265 $\mp$ 0.0001i
$(2,\pm1)$	$-$ 1.6180i	$\mp$1.6180i	$-$ 1.6180i	$\mp$1.6180i	$-$ 1.6180i	$\mp$1.6180i	$-$ 1.6164i	$-$0.0001 $\mp$ 1.8316i	0.0001 $-$ 1.6128i	$-$0.0001 $\mp$ 1.8275i
$(3,\pm1)$	$-$1.3537	$\mp$1.3537	$-$1.3537	$\mp$1.3537	$-$1.3537	$\mp$1.3537	$-$1.3537 $-$ 0.0002i	$\mp$1.2899 + 0.0001i	$-$1.3516 $-$ 0.0002i	$\mp$1.2875 + 0.0001i
$(20,-1)$	0.5538i	0.5538i	0.5538i	0.5538i	0.5538i	0.5538i	0.9305 + 11.2253i	0.3896 + 86.3633i	0.9663 + 8.0316i	0.3702 + 86.3789i
(25,1)	0.4965	$-$ 0.4965	21.7926 $-$ 0.6671i	0.5188 $-$ 0.1275i	$< 1e-8$	$-$0.5353	1.09e+04 + 2.3e+03i	9.8e+04 + 3.3e+02i	8.17e+03 + 2.36e+03i	9.8e+04 + 3.1e+02i
$\binom{n,}{m \neq \pm1}$	0	0	0	0	0	0	$< 1e-8$	$< 1e-8$	$< 1e-8$	$< 1e-8$

3.3.2 Expansion Coefficients for *z* Directed Hertzian Dipole

Hertzian dipole application is an important part to test success of the derived algorithm and to determine the most effective quadrature technique by comparing the results. Basic geometry of z directed Hertzian dipole is presented in Figure 3-8.

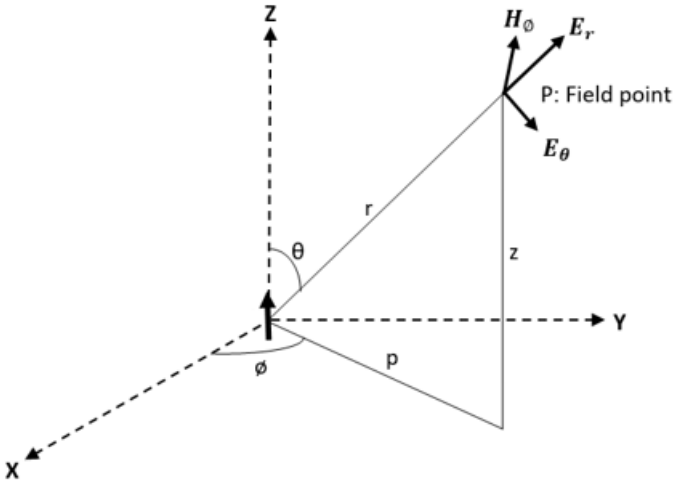

Figure 3-8: *z* directed Hertzian dipole geometry

E and ***H*** field expressions for an electric dipole excerpt from [9] are presented in equations (3.62), (3.63), (3.64) and (3.65) where ℓ is the length and I_0 is the current of the electric dipole.

$$H_r = H_\theta = E_\phi = 0 \tag{3.62}$$

$$H_\phi = \frac{jkI_0\ell \sin\theta}{4\pi r}\left[1 + \frac{1}{jkr}\right]e^{-jkr} \tag{3.63}$$

$$E_r = \frac{YI_0\ell \cos\theta}{2\pi r^2}\left[1 + \frac{1}{jkr}\right]e^{-jkr} \tag{3.64}$$

$$E_\theta = jY\frac{kI_0\ell \sin\theta}{4\pi r}\left[1 + \frac{1}{jkr} - \frac{1}{(kr)^2}\right]e^{-jkr} \tag{3.65}$$

The multipole coefficients of arbitrarily oriented Hertzian dipole (electric) in the matrix form can be written as given in equation (3.66)

$$\begin{bmatrix} b_{1,-1} \\ b_{1,0} \\ b_{1,1} \end{bmatrix} = jkZ \sqrt{\frac{2\pi}{3}} \begin{bmatrix} 1 & j & 0 \\ 0 & 0 & \sqrt{2} \\ 1 & -1 & 0 \end{bmatrix} \begin{bmatrix} p_x \\ p_y \\ p_z \end{bmatrix} \tag{3.66}$$

where $\boldsymbol{p} = p_x \boldsymbol{a_x} + p_y \boldsymbol{a_y} + p_z \boldsymbol{a_z}$ is the dipole moment.

Equation (3.66) states that, for a z directed Hertzian dipole (electric) presented in Figure 3-8, only b_{10} will exist and all other coefficients will be zero. For a Hertzian dipole directed in $\boldsymbol{p}$ direction with a current I_0 and length ℓ vector potential can be written as in equation (3.67)

$$\boldsymbol{A} = \frac{jk\mu}{4\pi} \boldsymbol{p} I_0 \, \ell \, \frac{e^{-jkr}}{kr} = \frac{-jk\mu}{4\pi} \boldsymbol{p} I_0 \, \ell \, \mathrm{h}_0^{(2)}(kr) \tag{3.67}$$

p_z can be defined as in equation (3.68)

$$p_z = \frac{-jkI_0 \, \ell}{4\pi} \tag{3.68}$$

Multipole expansion coefficients of z directed Hertzian dipole (electric) with four different quadrature techniques including MATLAB® integral2 function are listed in Table 3-4. Results of the quadrature techniques are compatible with theoretical one ($b_{10} = 61.3996$ which is calculated by using equations (3.66) and (3.68)) from the point of existence of only b_{10} and it can be observed that Gaussian and integral2 quadrature techniques give more precise result than Trapezoid and Simpson. Also, note that during the calculations; 315 θ, 629 ϕ grid points are chosen for Trapezoid and Simpson rule and 25 θ, 20 ϕ grid points are chosen for Gauss rule.

Table 3-4: Multipole coefficients for Hertzian dipole (electric)

(n,m)	**Analytical Value**		**integral2**		**Gauss**		**Trapezoid**		**Simpson**	
	a_{nm}	b_{nm}	a_{nm}	b_{nm}	a_{nm}	b_{nm}	a_{nm}	b_{nm}	a_{nm}	b_{nm}
(1,0)	0	61.3996	0	61.3996	0	61.3996	0	61.3924	0	61.3897
$\binom{m \neq 1,}{n \neq 0}$	0	0	0	0	0	0	0	0	0	0

$kr = 10$, I_0 =1, ℓ =1

Far field radiation pattern of Hertzian dipole by applying Gauss quadrature is presented in Figure 3-9 with three-dimensional radiation pattern and polar form of normalized E plane at $\phi = 0$. Truncation order is chosen as $N = 1$ with grid points of $\pi/30$ for both θ and ϕ.

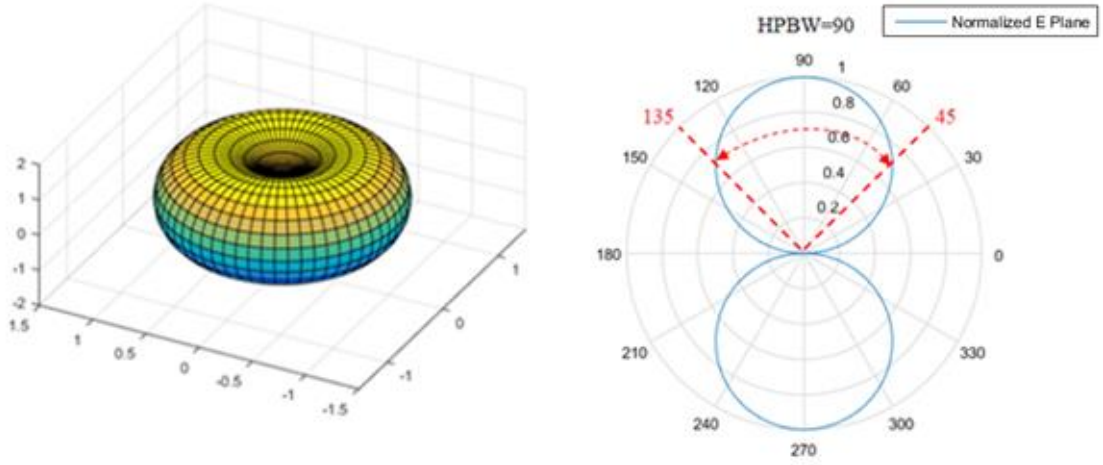

Figure 3-9: Far field radiation of z directed Hertzian (electric) dipole located at $(0,0,0)$ with Gauss quadrature

$\boldsymbol{E}$ and $\boldsymbol{H}$ field expressions for a magnetic dipole are based on [9] presented in equations (3.69), (3.70), (3.71), (3.72) and (3.73) where ℓ is the length and I_m is the current of magnetic dipole. Multipole expansion of magnetic dipole is listed in Table 3-5 and far field result is presented in Figure 3-10 with three dimensional radiation pattern and polar form of normalized E plane at $\phi = 0$.

$$E_r = E_\theta = H_\phi = 0 \tag{3.69}$$

$$H_r = \frac{I_m \ell \cos\theta}{2\pi r Y}\left[1 + \frac{1}{jkr}\right] e^{-jkr} \tag{3.70}$$

$$H_\theta = j\frac{kI_m \ell \sin\theta}{4\pi r Y}\left[1 + \frac{1}{jkr} - \frac{1}{(kr)^2}\right] e^{-jkr} \tag{3.71}$$

$$E_\phi = -j\frac{kI_m \ell \sin\theta}{4\pi r}\left[1 + \frac{1}{jkr}\right] e^{-jkr} \tag{3.72}$$

$$\begin{bmatrix} a_{1,-1} \\ a_{1,0} \\ a_{1,1} \end{bmatrix} = -k\sqrt{\frac{2\pi}{3}} \begin{bmatrix} 1 & j & 0 \\ 0 & 0 & \sqrt{2} \\ 1 & -j & 0 \end{bmatrix} \begin{bmatrix} m_x \\ m_y \\ m_z \end{bmatrix} \tag{3.73}$$

where $\boldsymbol{m} = m_x \boldsymbol{a_x} + m_y \boldsymbol{a_y} + m_z \boldsymbol{a_z}$ is the dipole moment and m_z is defined as:

$$m_z = \frac{-jkI_m \ell}{4\pi} \tag{3.74}$$

Equation (3.73) states that for a magnetic dipole only the coefficients $a_{1,0}$ exits with a theoretical value of $a_{10} = 0.1629i$ (calculated by equations (3.73) and (3.74)) and others are zero, as in the software output listed in Table 3-5.

Table 3-5: Multipole coefficients for Hertzian dipole (magnetic)

(n,m)	**Analytical Value**		**integral2**		**Gauss**		**Trapezoid**		**Simpson**	
	a_{nm}	b_{nm}	a_{nm}	b_{nm}	a_{nm}	b_{nm}	a_{nm}	b_{nm}	a_{nm}	b_{nm}
(1,0)	0.1629i	0	0.1629i	0	0.1629i	0	0.1628i	0	0.1624i	0
$\binom{m \neq 1,}{n \neq 0}$	0	0	0	0	0	0	0	0	0	0

$kr = 10$, I_m=1, $\ell = 1$

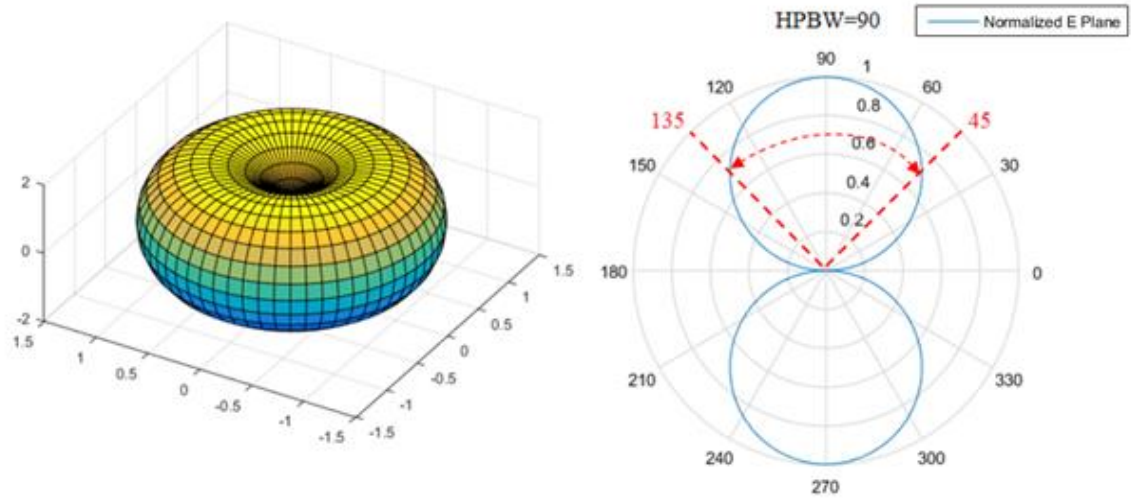

Figure 3-10: Far field radiation of z directed Hertzian (magnetic) dipole located at (0,0,0) with intagral2 quadrature

3.3.3 Expansion Coefficients for z Directed z Shifted Hertzian Dipole

For a Hertzian dipole located on the z axis at a distance d from the origin, the multipole coefficients are nonzero for any n and $m = 0$. The coefficients are zero for $m \neq 0$ since the ϕ symmetry is retained in the translation. It is possible to debug the developed code for different values of n for this case. Analytical expressions of the

coefficients are not available for this case. However, since the far field pattern will be same as for a dipole located at the origin, it is still possible to verify the numerical results.

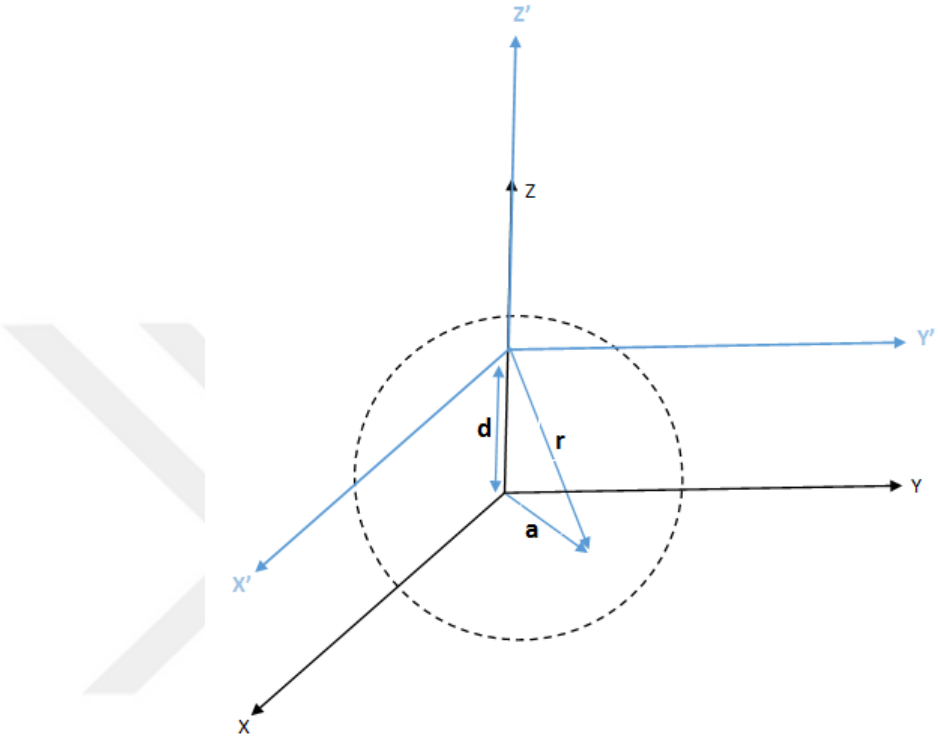

Figure 3-11: Hertzian dipole geometry shifted along the z axis

Numerical results of expansion coefficient for a Hertzian dipole located at $(0, 0, d)$ are listed in Table 3-6 and Table 3-7 for electric and magnetic dipole, respectively with four different quadrature techniques.

Table 3-6: Multipole coefficients for Hertzian dipole (electric) shifted on z axis

(n, m)	integral2		Gauss		Trapezoid		Simpson	
	a_{nm}	b_{nm}	a_{nm}	b_{nm}	a_{nm}	b_{nm}	a_{nm}	b_{nm}
(1,0)	0	$-0.0296 + 0.0037i$	0	$-0.0299 + 0.0037i$	0	$-0.0296 + 0.0037i$	0	$-0.0295 + 0.0037i$

(Table 3-6 continued)

(2,0)	0	$-0.0140 + 0.0157\text{i}$	0	$-0.0148 + 0.0165i$	0	$-0.0140 + 0.0156i$	0	$-0.0139 + 0.0156i$
(3,0)	0	$-0.0020 + 0.0165\text{i}$	0	$-0.0023 + 0.0188i$	0	$-0.0020 + 0.0164i$	0	$-0.0020 + 0.0164i$
(4,0)	0	$0.0024 + 0.0136i$	0	$0.0030 + 0.0179i$	0	$0.0024 + 0.0136i$	0	$0.0024 + 0.0136i$
(5,0)	0	$0.0015 + 0.0117i$	0	$0.0019 + 0.0200i$	0	$0.0015 + 0.0116i$	0	$0.0015 + 0.0116i$
(10,0)	0	$-6.1034e - 04 - 8.0824e - 04i$	0	$-6.5034e - 04 - 8.1324e - 04i$	0	$-6.0034e - 04 - 8.0924e - 04i$	0	$-6.0034e - 04 - 8.0924e - 04i$
(15,0)	0	$< 1e-7$	0	$< 1e-7$	0	$< 1e-7$	0	$< 1e-7$
(20,0)	0	$< 1e-10$	0	$< 1e-10$	0	$< 1e-10$	0	$< 1e-10$
$\binom{n,}{m \neq 0}$	0	0	0	0	0	0	0	0

$kr = 10, I_0 = 1, \ell = 1 \;\; a = 1.5, d = 1$

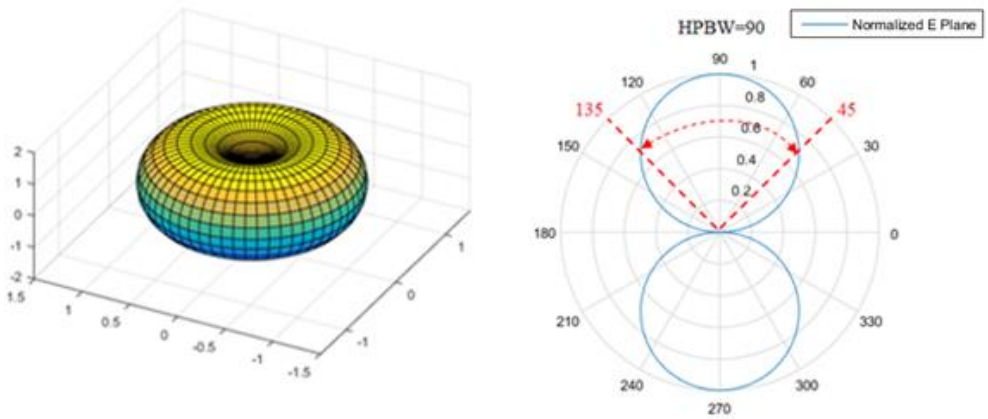

Figure 3-12: Far field radiation of z directed and z shifted Hertzian (electric) dipole located at $(0,0,d)$ with Trapezoid quadrature

Table 3-7: Multipole coefficients for Hertzian dipole (magnetic) shifted on z axis

(n, m)	**integral2**		**Gauss**		**Trapezoid**		**Simpson**	
	a_{nm}	b_{nm}	a_{nm}	b_{nm}	a_{nm}	b_{nm}	a_{nm}	b_{nm}
(1,0)	$-0.1834 - 1.1229i$	0	$-0.1834 - 1.1229$i	0	$-0.1835 - 1.1229$i	0	$-0.1838 - 1.1223$i	0
(2,0)	$-0.1288 - 0.2924i$	0	$-0.1288 - 0.2924i$	0	$-0.1207 - 0.2915i$	0	$-0.1207 - 0.2913i$	0
(3,0)	$-0.0843 - 0.0522i$	0	$-0.0843 - 0.0522i$	0	$-0.0862 - 0.0522i$	0	$-0.0866 - 0.0522i$	0
(4,0)	$-0.0440 - 0.0053i$	0	$-0.0440 - 0.0053i$	0	$-0.0443 - 0.0053i$	0	$-0.0440 - 0.0053i$	0
(5,0)	$-0.0225 - 0.0016i$	0	$-0.0225 - 0.0016i$	0	$-0.0227 - 0.0016i$	0	$-0.0226 - 0.0016i$	0
(15,0)	$< 1e-7$	0	$< 1e-7$	0	$< 1e-7$	0	$< 1e-7$	0
(20,0)	$< 1e-10$	0	$< 1e-10$	0	$< 1e-10$	0	$< 1e-10$	0
$\binom{n,}{m \neq 0}$	0	0	0	0	0	0	0	0

$kr = 10, I_m = 1, \ell = 1, a = 1.5, d = 1$

3.3.4 Expansion Coefficients for x Directed Hertzian Dipole

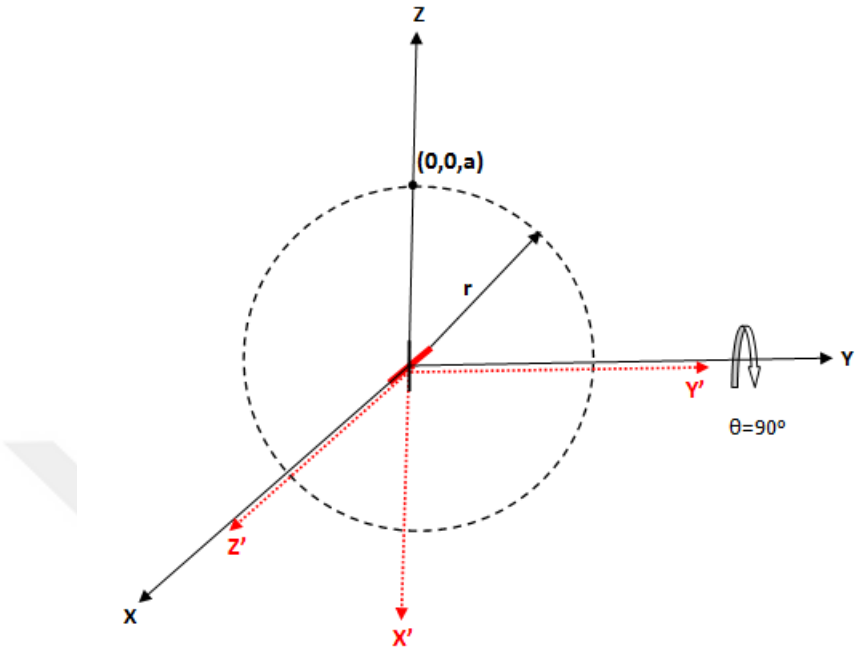

Figure 3-13: Hertzian dipole geometry directed on x axis

In sections 3.3.2 and 3.3.3, z directed Hertzian dipole located at $(0,0,0)$ and $(0,0,d)$ were analyzed to verify the developed code by computing the multipole coefficients from a known field. In this section x directed Hertzian dipole located at the origin is analyzed. As shown in Figure 3-13, z directed dipole can be translated to an x directed dipole by applying 90^{o} rotation around the y axis in clockwise direction and coordinate rotation matrix for this rotation is given in equation (3.75) (See Appendix A)

$$\begin{bmatrix} x' \\ y' \\ z' \end{bmatrix} = \begin{bmatrix} \cos\theta & 0 & -\sin\theta \\ 0 & 1 & 0 \\ \sin\theta & 0 & \cos\theta \end{bmatrix} \begin{bmatrix} x \\ y \\ z \end{bmatrix} \tag{3.75}$$

for $\theta = 90^{o}$ rotation matrix reduces to

$$\begin{bmatrix} x' \\ y' \\ z' \end{bmatrix} = \begin{bmatrix} 0 & 0 & -1 \\ 0 & 1 & 0 \\ 1 & 0 & 0 \end{bmatrix} \begin{bmatrix} x \\ y \\ z \end{bmatrix} \tag{3.76}$$

Expansion coefficients of the x directed Hertzian dipole are calculated by developed code with four different quadrature techniques as in Table 3-8 and far field radiation is presented in Figure 3-14.

Table 3-8: Multipole coefficients for x directed Hertzian (electric) dipole

(n, m)	**integral2**		**Gauss**		**Trapezoid**		**Simpson**	
	a_{nm}	b_{nm}	a_{nm}	b_{nm}	a_{nm}	b_{nm}	a_{nm}	b_{nm}
(1,1)	0	-0.0014 − 0.0116i	0	−0.0014 − 0.0117i	0	−0.0014 − 0.0116i	0	−0.0014 − 0.0116i
$(1, -1)$	0	0.0014 + 0.0116i	0	0.0014 + 0.0117i	0	0.0014 + 0.0116i	0	0.0014 + 0.0116i
$\binom{n \neq 1,}{m \neq \pm 1}$	0	0	0	0	0	0	0	0

$kr = 10, I_0 = 1, \ell = 1$

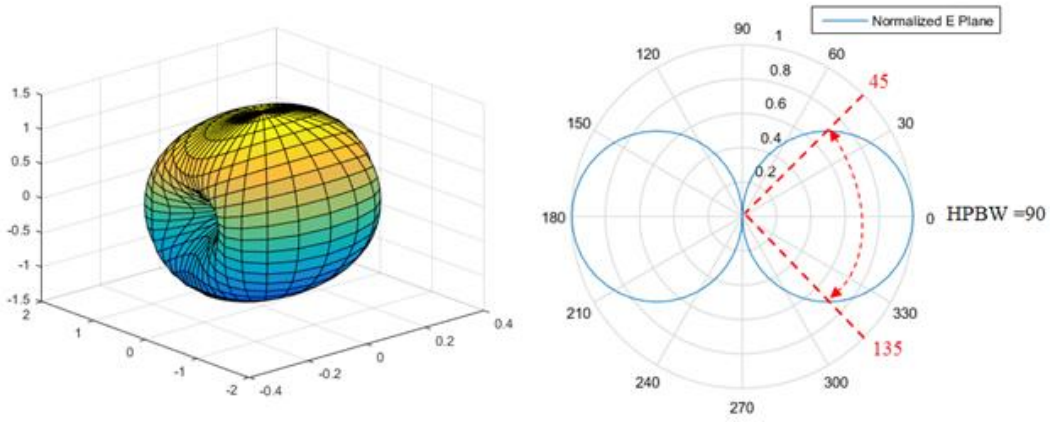

Figure 3-14: Far field radiation of x directed Hertzian (electric) dipole located at $(0,0,0)$ with Simpson quadrature

CHAPTER 4

NEAR FIELD TO FAR FIELD TRANSFORMATION OF SPHERICALLY SCANNED DATA

4.1 Far Field Transformation of Experimental Data Using Trapezoid and Simpson Quadrature Techniques

Near field data that will be transformed to far field is acquired in anechoic chamber of METU which is capable of spherical scanning. Measurement setup of METU is based on Figure 4-1 with the stationary probe and necessary rotations are implemented by test antenna both in θ and ϕ axis and χ is the probe rotation angle corresponds to two orthogonal components of electric field E_θ and E_ϕ.

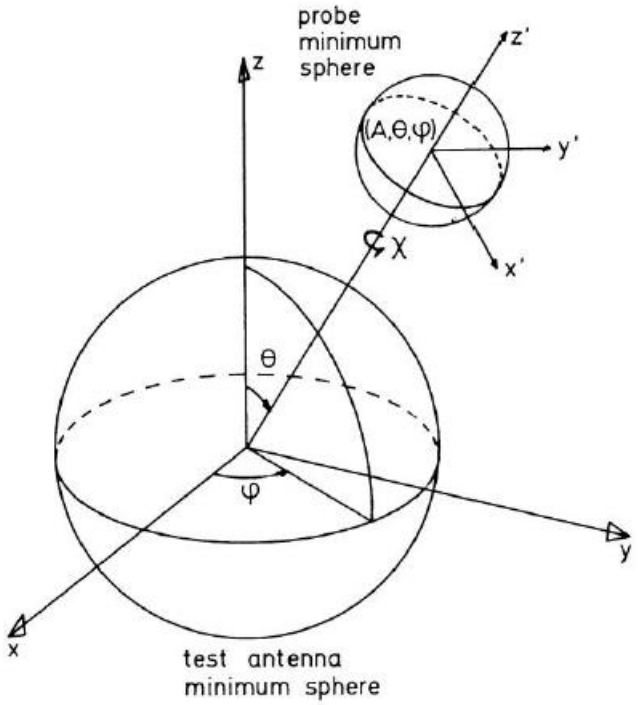

Figure 4-1: Test antenna and probe geometry [1]

Developed code for calculation of multipole coefficients and far field radiations has been verified by applying to plane wave and Hertzian dipole antennas in Chapter 3. This chapter includes the application of far field transformation algorithm to a spherical scanned near field data which is acquired in METU anechoic chamber with a uniform spacing in both azimuth ($\phi = 0{:}\,360^{o}$) and elevation ($\theta = 0{:}\,180^{o}$) axis with a resolution of 1.5^{o} .

The measurements are taken at a distance of 2.4 m from the test antenna with the probe antenna $ASY - CWG - S - 058$ shown in Figure 4-2 which is a linearly polarized antenna. The test antenna has a radius of 0.525 m, thus the measurement distance corresponds to radiating near field of the antenna. The radius of the test antenna implies that multipole expansion of its field can be truncated at $N = 2kr = 160$.

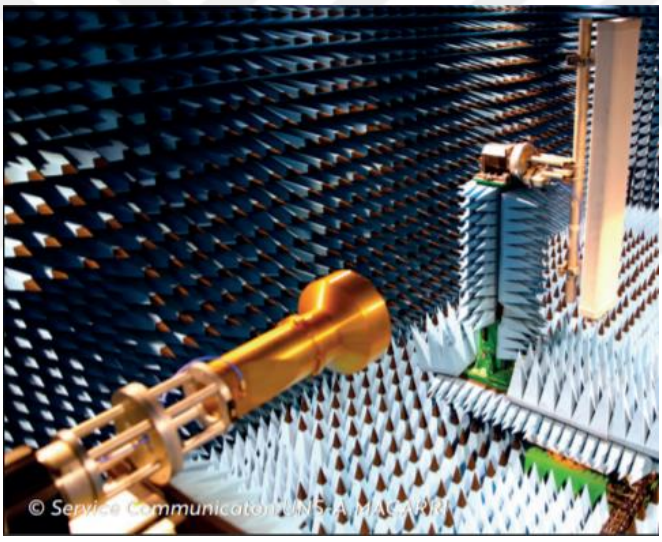

Figure 4-2: Near field probe antenna $ASY - CWG - S - 058$

Near field measurement of a reflector type antenna has been performed in the spherical near field measurement setup of METU and the two orthogonal components of this measurement are considered to be the E_θ and E_ϕ components of the field which are presented in Figures (4.3), (4.4), (4.5) ,(4.6) at $\phi = 0^{o}$ and $\phi = 90^{o}$.

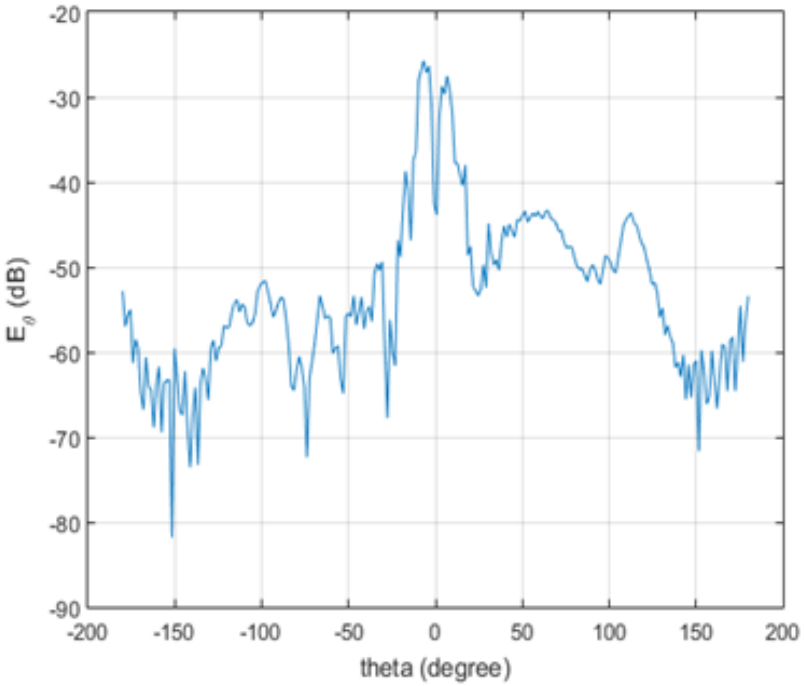

Figure 4-3: Near field $E_\theta$versus θ at $\phi = 0^o$ and $f = 7.25\ GHz$

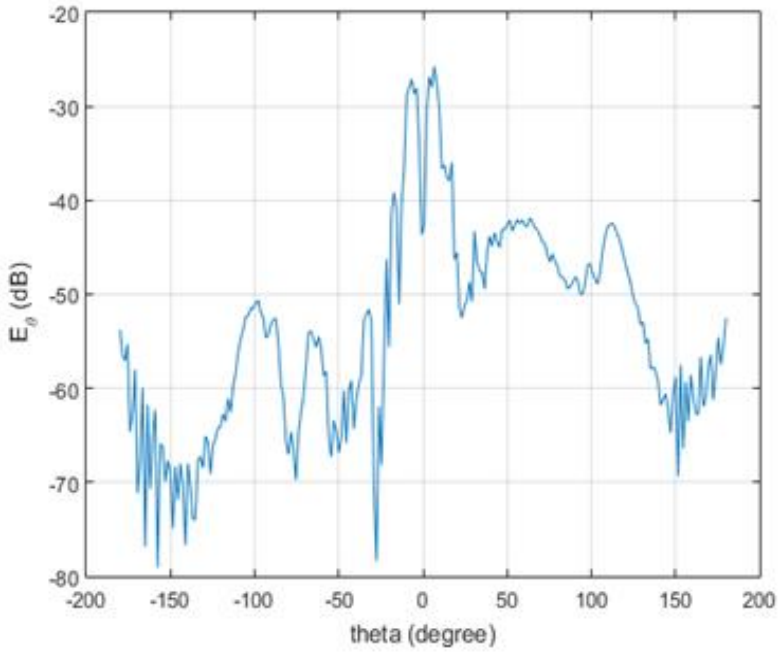

Figure 4-4: Near field $E_\theta$versus θ at $\phi = 90^o$ and $f = 7.25\ GHz$

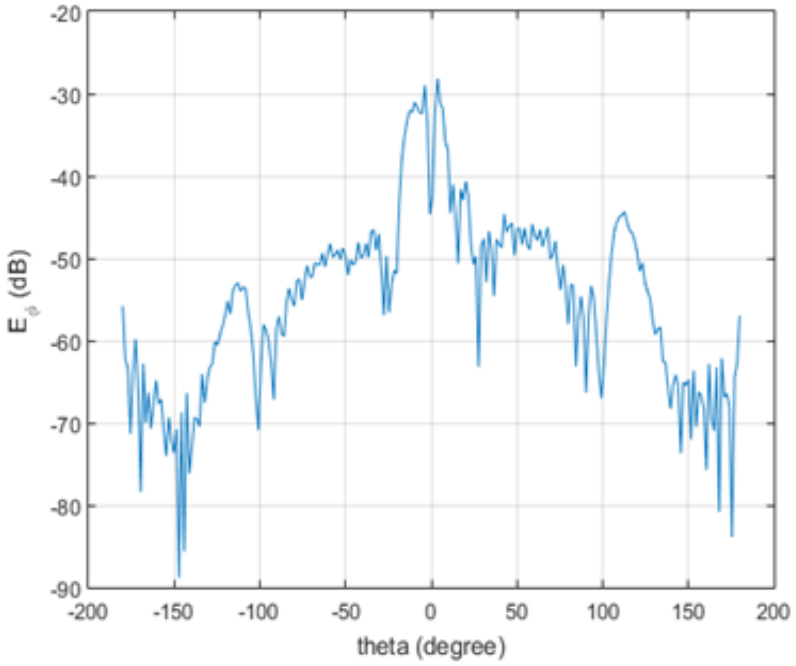

Figure 4-5: Near field E_ϕ versus θ at $\phi = 0^\circ$ and $f = 7.25\ GHz$

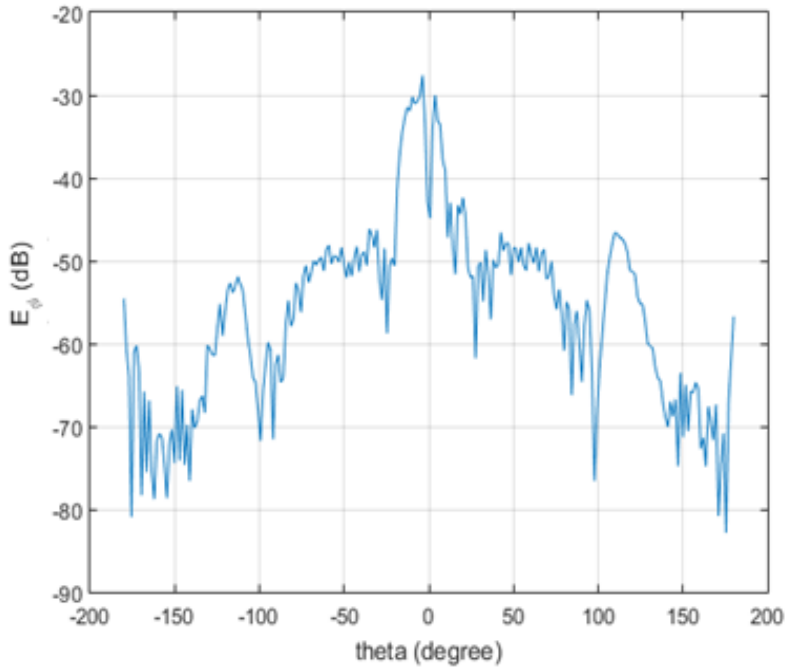

Figure 4-6: Near field E_ϕ versus θ at $\phi = 90^\circ$ and $f = 7.25\ GHz$

In this section, aperture of the probe is ignored and it is assumed that the probe measures radiation field of test antenna directly. The multipole coefficients can thus be calculated by using equations (3.37), (3.40) and the measurement data. Note that only the tangential components of the electric field are needed and the two measured components, namely E_θ and E_ϕ.

Once the multipole coefficients are determined, far field of the test antenna is obtained easily by using the asymptotic forms of the radial functions in the multipole expansion. This is basically the spherical near field to far field transformation algorithm.

First step of transformation algorithm is to calculate the multipole coefficients given in equations (3.37) and (3.40) by applying the quadrature techniques which have been explained in Chapter 3 for numerical integration. Uniformly spaced characteristic of near field data leads to usage of Newton Cotes techniques instead of Gauss quadrature technique which determines the proper integration points instead of uniform spacing. In this thesis, Trapezoid and Simpson from Newton Cotes techniques are chosen to calculate the numerical integration part of multipole expansion coefficients.

Second step of transformation algorithm is to determine the far field $\boldsymbol{E}$ given in the equation (3.25) by using the multipole expansion coefficients calculated in the first part and asymptotic form of vector wave functions $\boldsymbol{M}$ and $\boldsymbol{N}$. Spherical wave expansion presentation of an $\boldsymbol{E}$ field given in equation (3.25) requires the infinite summation over n which is not feasible for numerical calculations. This computational constraint necessitates to truncate n at a value of N which is generally in the order of $2kr$ where k is wave number and r is the radius of minimum sphere that encloses the test antenna.

In practice, the measuring probe has an aperture and therefore the quantity measured by the probe is a weighted integral of the electric field radiated by the test antenna over the probe aperture. Taking this fact into account is probe compensation and this is considered in Chapter 5. In fact, presence of the probe also affects the field radiated by the test antenna, but this effect is ignored in near field to far field transformation

algorithms. Near field measurements are always done in the radiating near field to ensure that this effect is negligible.

If the measuring probe was a Hertzian dipole, the measured field would exactly be the electric field at the location of the probe, again assuming that the probe does not change the radiated field. For a Hertzian dipole, this assumption would be quite accurate since a Hertzian dipole is a point antenna. However, Hertzian dipole is a hypothetical antenna and we can only use electrically small dipoles as an approximation to such an antenna. In practice, electrically small dipoles are not used since

a) the electrically small dipole is an inefficient antenna and therefore the received signal would be very small and measurement accuracy would be degraded by noise,
b) the electrically small dipole antenna is an open structure and, if not impossible, it is quite difficult to have low cross polarization values.

However, Hertzian dipole probe assumption can hypothetically be used with the measured data and the near field to far field transformation can be applied under this assumption.

The results obtained in this section are compared to those obtained by the SNIFT code [26] available in the METU spherical near field measurement range. This code is developed by TICRA and is a part of the METU antenna range. In the TICRA SNIFT code, if the measurement probe is chosen as Hertzian dipole, probe compensation is not included and comparison becomes possible.

Following section of this chapter includes the far field radiation output of the developed code based on Trapezoid and Simpson quadrature rules. Before starting the near field data processing, truncation order N must be determined for the infinite sum given in equation (3.25). This order should be $N = 2kr = 160$ with wave number k and the test antenna radius r for the given measurement setup. Figure 4-7 shows the software output by processing the near field data given in Figure 4-3 with Trapezoid

rule and truncation order of $N = 160$. Also, this figure includes the near field to far filed transformation result of SNIFT code and it can be observed that SNIFT code and developed code are in good agreement with the truncation order of $N = 160$

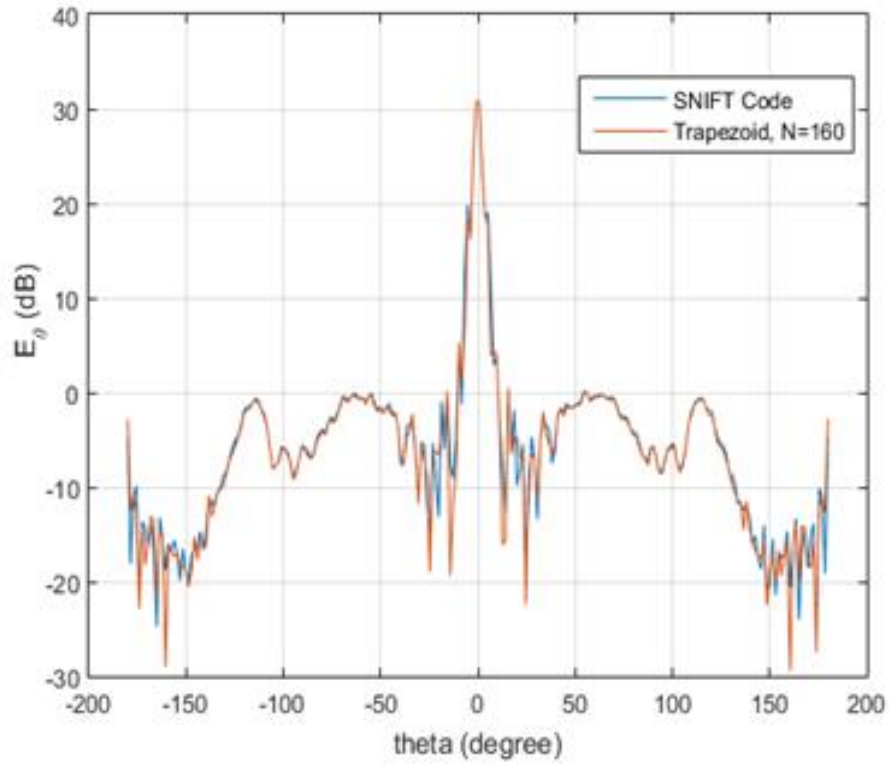

Figure 4-7: Far field E_θ obtained from near field to far field transformation algorithm with Trapezoid quadrature and truncation order $N = 160$ at $\phi = 0^o$ and $f = 7.25\ GHz$

Determining the number of terms that must be kept in the summation properly has a high importance for the near field to far field transformation algorithm's success. Including fewer terms than required can result in numerical inaccuracies, on the other hand including too many terms than required can also cause numerical inaccuracies because of the oscillation of spherical Hankel functions for exponentially large values.

Far field outputs of the derived algorithm with $N = 50$ and $N = 200$ are presented in Figure 4-8 and Figure 4-9, respectively for near field data given in Figure 4-3. Output of SNIFT code for same near field data is also given in same figure.

The discrepancy between two results in Figure 4-8 can be attributed to have less N than required and in Figure 4-9 can be attributed to include too many terms than required. Both figures verify the numerical inaccuracies caused by improper truncation order.

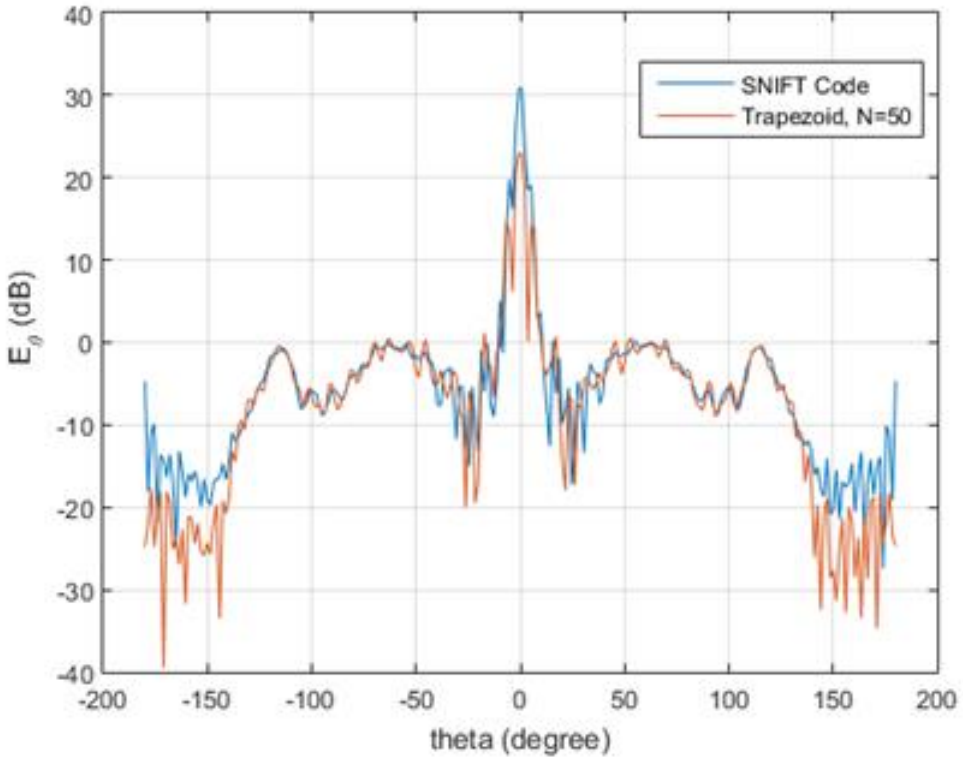

Figure 4-8: Far field E_θ obtained from near field to far field transformation algorithm with Trapezoid quadrature and truncation order $N = 50$ at $\phi = 0^o$ and $f = 7.25\ GHz$

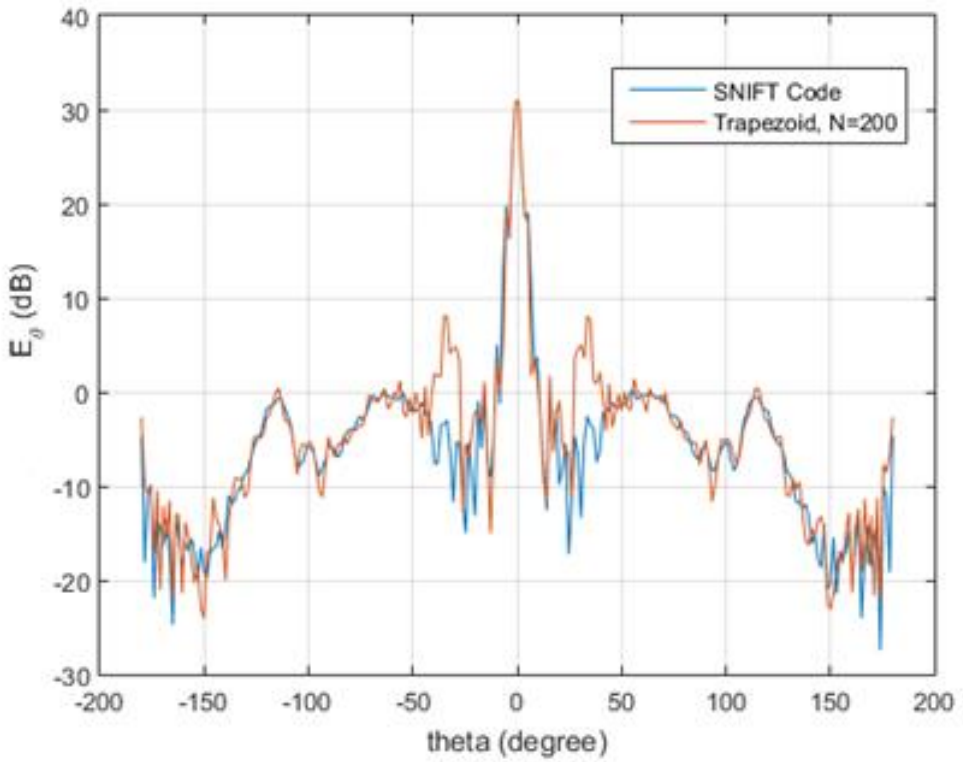

Figure 4-9: Far field E_θ obtained from near field to far field transformation algorithm with Trapezoid quadrature and truncation order $N = 200$ for $\phi = 0^o$ and $f = 7.25\ GHz$

Result of the analysis for truncation order specified above shows that $N = 160$ is the most appropriate truncation order which fits with SNIFT code outputs. So, near field to far field transformation will be performed with the truncation order of 160 in the following part.

Far field transformation of near field data shown in Figures (4.2), (4.3), (4.4) and (4.5) is also performed by using developed transformation algorithm with Trapezoid and Simpson quadrature rules. Figure 4-10 shows the far field E_θ at $\phi = 0$ obtained using near field to far field transformation algorithm with Trapezoid and Simpson quadrature and also output of SNIFT code is given on the same figure. It can be observed that, although Trapezoid rule and SNIFT code are in good agreement, Simpson differs from these two results. Also, Simpson method do es not give a smooth

result as in Trapezoid and SNIFT code which can be the result of improper integrand for approximating with second order polynomial which is the basic idea of Simpson rule. Namely, high oscillations of spherical Hankel functions cannot be approximated with a simple polynomial properly.

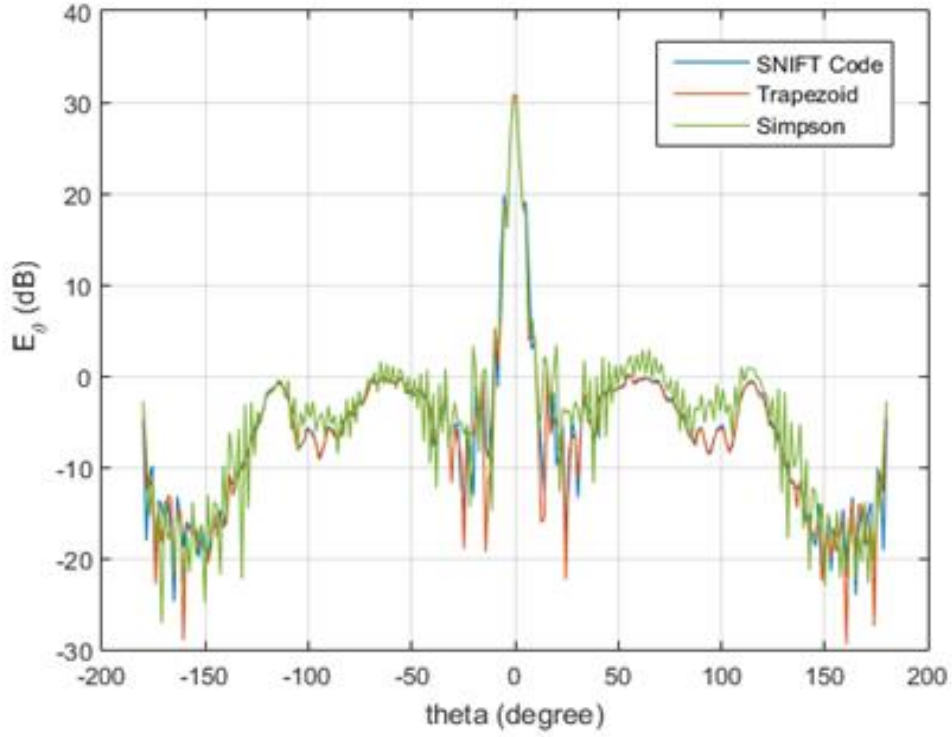

Figure 4-10: Comparison of far field E_θ obtained from near field to far field transformation algorithm with Trapezoid and Simpson quadrature at $\phi = 0^o$ and $f = 7.25\ GHz$

The transformed far field E_θ in $\phi = 90$ plane of the near field data given in Figure 4-3 is shown in Figure 4-11 for two quadrature rules and it can be observed that Trapezoid and SNIFT are in good agreement but Simpson has some error as in Figure 4-10.

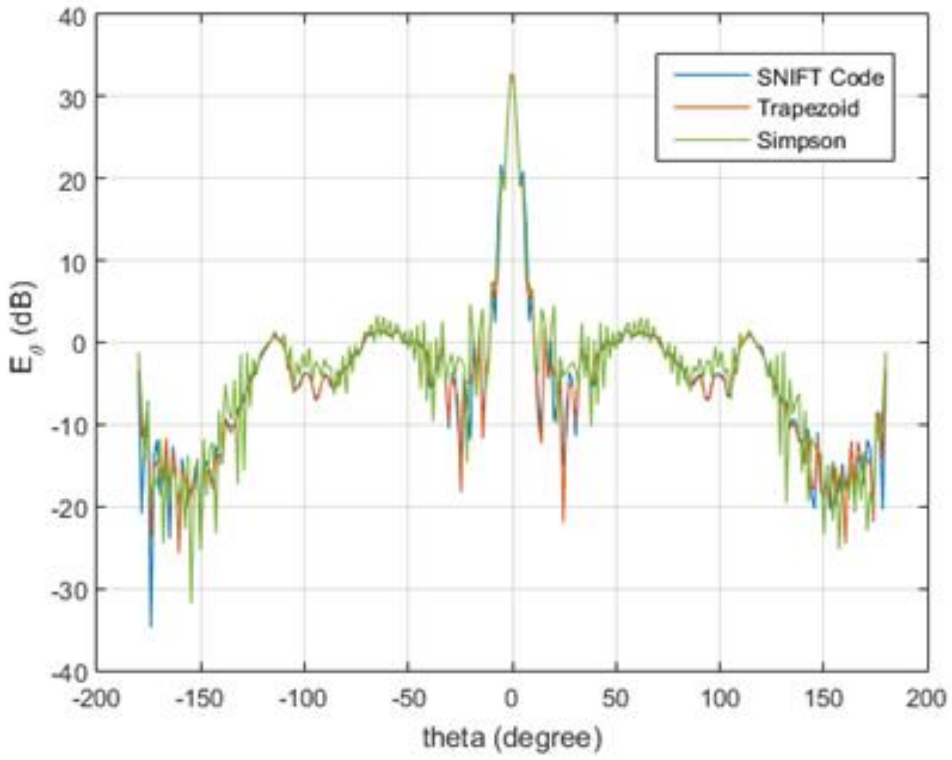

Figure 4-11: Comparison of far field E_θ obtained from near field to far field transformation algorithm with Trapezoid and Simpson quadrature at $\phi = 90^o$ and $f = 7.25\ GHz$

The transformed far field E_ϕ at $\phi = 0^o$ is presented in Figure 4-12 for three quadrature methods. SNIFT and Trapezoid rules are in good agreement. Smoothness problem of Simpson is seen again for E_ϕ and this leads to conclusion that, it does not depend on the processed field component E_θ or E_ϕ, it is related to the unsuitable quadrature technique for the numerical evaluation of integrands given in (3.37) and (3.40).

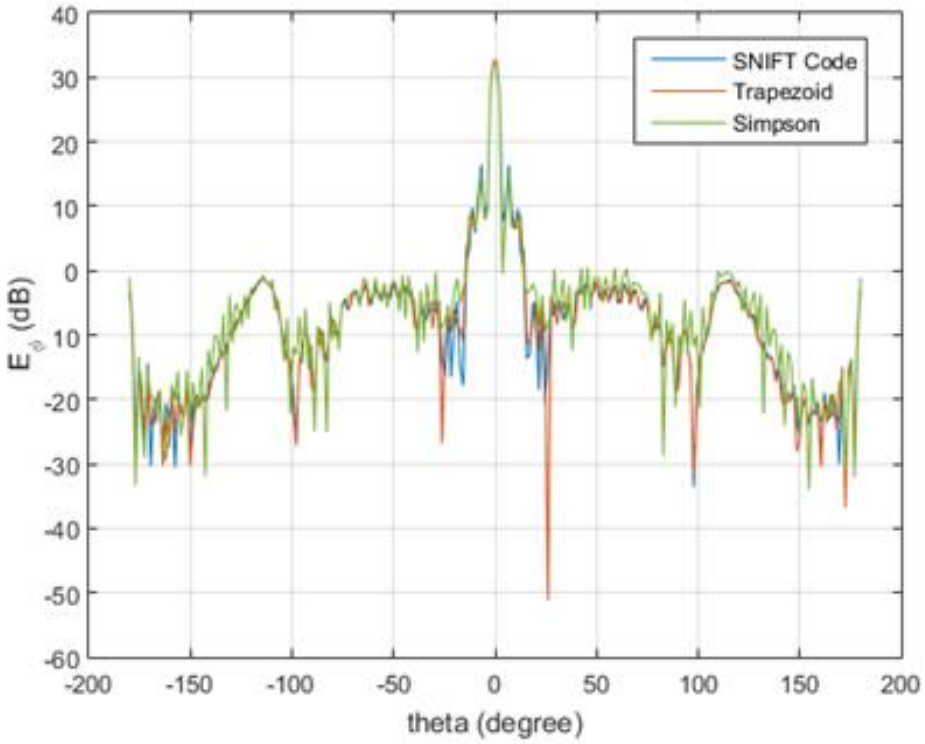

Figure 4-12: Comparison of far field E_ϕ obtained from near field to far field transformation algorithm with Trapezoid and Simpson quadrature E_ϕ at $\phi = 0^\circ$ and $f = 7.25\ GHz$

The transformed far field E_ϕ at $\phi = 90^\circ$ is presented in Figure 4-13 for three quadrature methods and Simpson is again not successful as Trapezoid. SNIFT and Trapezoid rules are in good agreement.

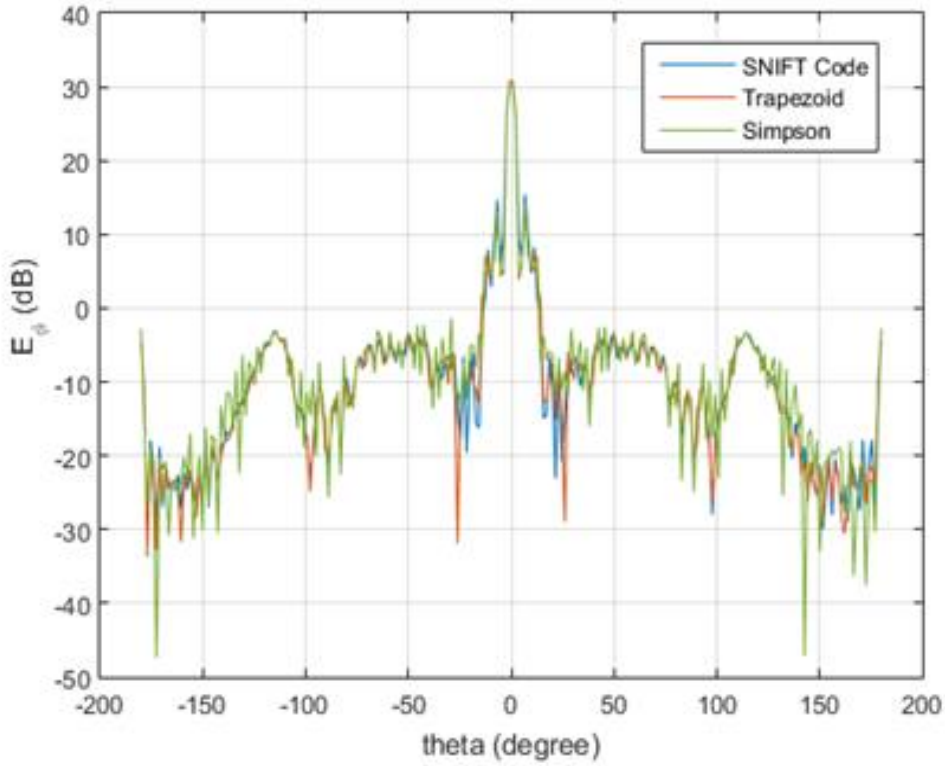

Figure 4-13: Comparison of far field E_{ϕ} obtained from near field to far field transformation algorithm with Trapezoid and Simpson quadrature at $\phi = 90^{o}$ and $f = 7.25\ GHz$

Far field transformation of experimental near field data is presented through Figure 4-7 to Figure 4-13 at $\phi = 0^{o}$ and $\phi = 90^{o}$. Figure 4-14, Figure 4-15 and Figure 4-16 show the three dimensional radiation including all θ and ϕ angles for SNIFT, Trapezoid and Simpson, respectively. From the comparison of these three figures, it can be concluded that Trapezoid quadrature rule is more compatible than Simpson for the experimental data processed in this study.

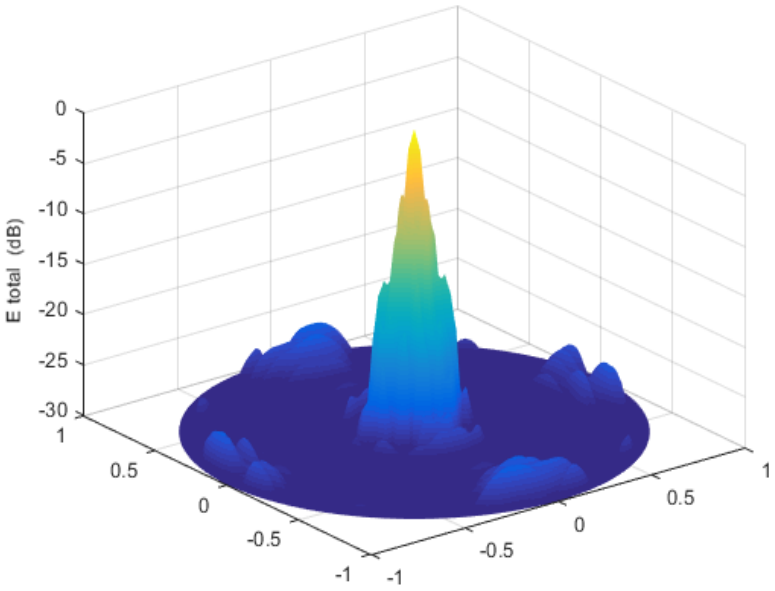

Figure 4-14: Total E field obtained from near field to far field transformation algorithm with SNIFT at $f = 7.25\ GHz$

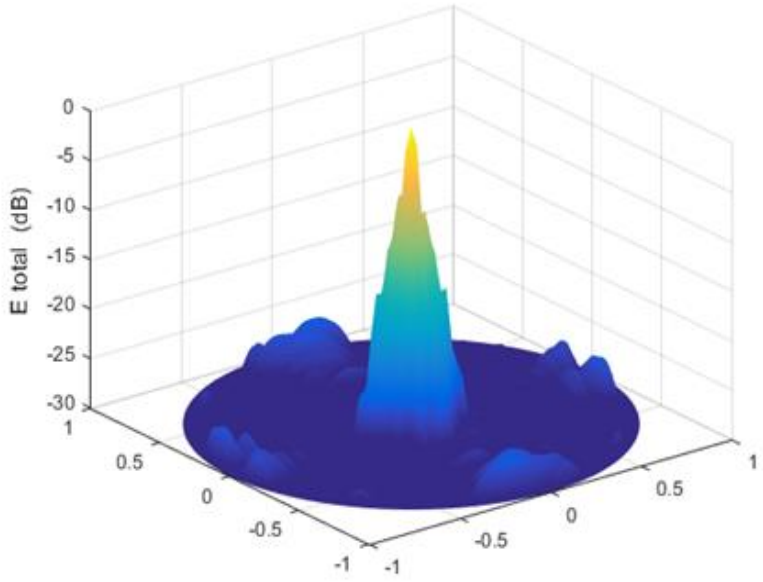

Figure 4-15: Total E field obtained from near field to far field transformation algorithm with Trapezoid quadrature at $f = 7.25\ GHz$

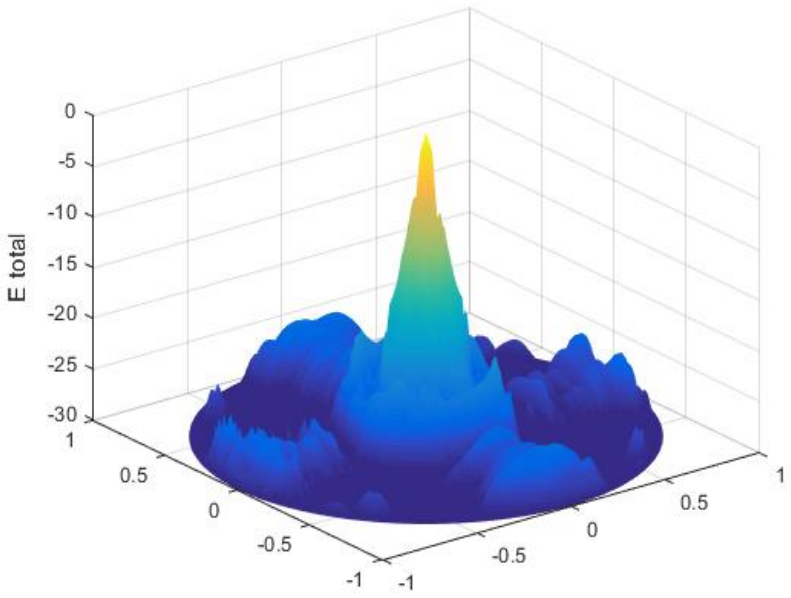

Figure 4-16: Total E field obtained from near field to far field transformation algorithm with Simpson quadrature at $f = 7.25\ GHz$

4.2 Analysis of Near Field to Far Field Transformation Algorithm

Far field transformation with Trapezoid and Simpson techniques is applied to near field E_θ and E_ϕ data acquired in METU anechoic chamber and these transformations are also compared with the result of SNIFT code in the foregoing parts of this chapter. All these studies can be concluded as;

- Two orthogonal components of E_θ and E_ϕ fields are processed using the far field transformation by applying the quadrature methods to calculate multipole coefficients numerically,
- Determining the truncation order for infinite sum given in (3.25) is a critical step of the transformation to get a more accurate far field E_θ, E_ϕ. This study shows that this order must be in the order of $2kr$ which equals to approximately 160 for above calculations,

Far field transformation results presented in above figures show that Trapezoid rule is more convenient and accurate than Simpson rule for the integrands given in (3.37) and (3.40). And this leads to conclusion that approximating integrals given in (3.37) and (3.40) with the summation of trapezoids under the curve of function gives more precise result than approximating these integrands with a second order polynomial. High oscillating characteristic of spherical Hankel functions cannot be approximated with a simple polynomial properly,

- SNIFT code was a reliable tool to verify the result of this study and comparison results given in above figures show that output of this study is mostly compatible with SNIFT transformation,
- Error is inevitable result for this study because of the truncation of the infinite sum over n in equations (3.25) and the numerical calculation of integrals in equations (3.37) and (3.40) instead of analytical calculations.

Also note that, all studies have been performed without considering the probe effect in this chapter and compensation of this effect will be analyzed in the following chapter.

CHAPTER 5

PROBE COMPANSATION IN NEAR FIELD TO FOR FIELD TRANSFORMATION

5.1 Basic Theory of Spherical Probe Compensation

Following derivations for probe compensation is based on [21] and [28]. When the probe antenna is introduced to measure field generated by test antenna, primary field is affected by the probe antenna and there is no method proposed in the literature to take this effect into account. However, this effect is negligible if the probe antenna is outside the reactive near field of the antenna under test. The probe antenna responds to a weighted sum of the field on its aperture and therefore it cannot measure the field at a point in space. This effect can be compensated if the properties of the probe antenna are known. It is the purpose of this section to derive a transformation algorithm that includes probe compensation, by means of well known Lorentz reciprocity theorem.

Basic spherical probe compensation geometry is presented in Figure 5-1. Fields generated by test antenna *A* is to be measured by probe antenna *B* over a spherical surface. *O* is the origin of test antenna coordinate system, *O'* is the origin of probe antenna coordinate system and *O''* is the origin of double primed coordinate system whose axes are parallel to the probe antenna coordinate system. In Figure 5-1, let Σa be a sphere that encloses the test antenna with a current source $\boldsymbol{J}_a(\boldsymbol{r})$ and the fields radiated by the test antenna are denoted by $\boldsymbol{E}_a(\boldsymbol{r})$, $\boldsymbol{H}_a(\boldsymbol{r})$. These fields are incident on the probe antenna and the radiated fields of the probe antenna are denoted as $\boldsymbol{E}_b(\boldsymbol{r}')$ and $\boldsymbol{H}_b(\boldsymbol{r}')$ when the current source of $\boldsymbol{J}_b(\boldsymbol{r}')$ is enabled, $\boldsymbol{r}'$ is measured with respect to *O'*.

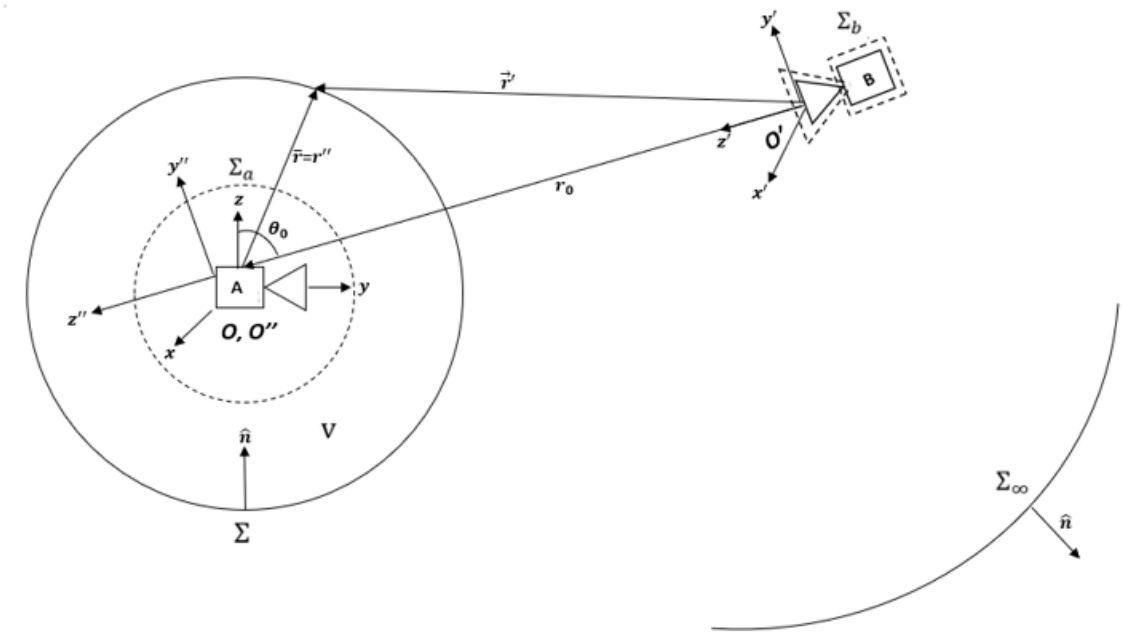

Figure 5-1: Spherical probe compensations geometry [21]

The probe antenna can be represented as Thevenin equivalent source to define the open circuit voltage, V_{oc} induced at its terminals by the incident wave, $\boldsymbol{E}_a(\boldsymbol{r})$. The open circuit voltage, V_{oc} depends on the amplitude of incident field. The reciprocity theorem will be used to develop formulas for the probe antenna open circuit voltage, V_{oc} in terms of transmit equivalent current model. Because, the receiving characteristics of an antenna can be related with its transmitting characteristics by reciprocity theorem. The current source of probe antenna, $\boldsymbol{J}_b(\boldsymbol{r}')$ will be used to measure the strength of the fields radiated by test antenna, $\boldsymbol{E}_a(\boldsymbol{r})$ and this is called as reaction. The reaction between the probe antenna current source, $\boldsymbol{J}_b(\boldsymbol{r}')$ and the fields radiated by test antenna, $\boldsymbol{E}_a(\boldsymbol{r})$ is defined as in equation (5.1). For reaction analysis it is assumed that, both the source of the probe and test antennas are not impressed at the same time.

$$\langle \boldsymbol{J}_b(\boldsymbol{r}') , \boldsymbol{E}_a(\boldsymbol{r}) \rangle = \int_V \boldsymbol{J}_b(\boldsymbol{r}') . \boldsymbol{E}_a(\boldsymbol{r})\, dV \tag{5.1}$$

The test and probe antennas can be called as reciprocal if they satisfy the equation 5.2, in case of no magnetic sources are available.

$$\langle \boldsymbol{J}_a(\boldsymbol{r}) , \boldsymbol{E}_b(\boldsymbol{r}') \rangle = \langle \boldsymbol{J}_b(\boldsymbol{r}') , \boldsymbol{E}_a(\boldsymbol{r}) \rangle \tag{5.2}$$

The reciprocity theorem can be derived as in equation (5.4) by using reciprocity property given in equation (5.2) and inserting Maxwell equations to replace the current sources and then applying vector calculus.

$$\langle \boldsymbol{J}_a(\boldsymbol{r}) , \boldsymbol{E}_b(\boldsymbol{r}') \rangle - \langle \boldsymbol{J}_b(\boldsymbol{r}') , \boldsymbol{E}_a(\boldsymbol{r}) \rangle = \int_V [\boldsymbol{J}_a(\boldsymbol{r}) . \boldsymbol{E}_b(\boldsymbol{r}') - \boldsymbol{J}_b(\boldsymbol{r}') . \boldsymbol{E}_a(\boldsymbol{r})] dV \tag{5.3}$$

$$\langle \boldsymbol{J}_a(\boldsymbol{r}) , \boldsymbol{E}_b(\boldsymbol{r}') \rangle - \langle \boldsymbol{J}_b(\boldsymbol{r}') , \boldsymbol{E}_a(\boldsymbol{r}) \rangle = \int_{\Sigma} [\boldsymbol{E}_a(\boldsymbol{r}) \times \boldsymbol{H}_b(\boldsymbol{r}') - \boldsymbol{E}_b(\boldsymbol{r}') \times \boldsymbol{H}_a(\boldsymbol{r})]\, dS \tag{5.4}$$

The open circuit voltage of probe antenna for a z' aligned infinitesimal current source, $\boldsymbol{J}_b(\boldsymbol{r}')$ can be derived by using the reaction of $\boldsymbol{J}_b(\boldsymbol{r}')$ and $\boldsymbol{E}_a(\boldsymbol{r})$.

$$\langle \boldsymbol{J}_b(\boldsymbol{r}') , \boldsymbol{E}_a(\boldsymbol{r}) \rangle = \int_V \boldsymbol{J}_b(\boldsymbol{r}') . \boldsymbol{E}_a(\boldsymbol{r})\, dV \tag{5.5}$$

$$\langle \boldsymbol{J}_b(\boldsymbol{r}') , \boldsymbol{E}_a(\boldsymbol{r}) \rangle = \int_V [-I_b \boldsymbol{z} \delta(x') \delta(y')] . \boldsymbol{E}_a(\boldsymbol{r})\, dV \tag{5.6}$$

$$\langle \boldsymbol{J}_b(\boldsymbol{r}') , \boldsymbol{E}_a(\boldsymbol{r}) \rangle = -I_b \int_{z_1}^{z_2} \boldsymbol{E}_a(\boldsymbol{r})\, dl \tag{5.7}$$

$$\langle \boldsymbol{J}_b(\boldsymbol{r}') , \boldsymbol{E}_a(\boldsymbol{r}) \rangle = I_b\, V_{oc}(b) \tag{5.8}$$

Similarly, it can be shown that

$$\langle \boldsymbol{J}_a(\boldsymbol{r}') , \boldsymbol{E}_b(\boldsymbol{r}) \rangle = I_a \, V_{oc}(a) \tag{5.9}$$

By reciprocity theorem, the two reaction integrals are equal as stated in equation (5.10)

$$I_a \, V_{oc}(a) = I_b \, V_{oc}(b) \tag{5.10}$$

$V_{oc}(b)$ is the open circuit voltage induced across the terminals of probe antenna. $V_{oc}(b)$ represents the energy received by probe antenna from an incident wave, $\boldsymbol{E}_a(\boldsymbol{r})$ and its level depends on the amplitude, polarization and direction of arrival of incident wave. The radiation pattern of the test antenna can be calculated from the measurement of the power at the terminals of the probe antenna which is proportional with $|V_{oc}(b)|^2$.

Let $P_B(r_0)$ represents the measured signal by the probe antenna which is proportional to the open circuit received voltage when the test antenna is radiating. Lorentz reciprocity theorem states that,

$$\oint_{\Sigma} (\boldsymbol{E}_a \times \boldsymbol{H}_b - \boldsymbol{E}_b \times \boldsymbol{H}_a) \cdot \hat{n} \, dS = P_B(\boldsymbol{r_0}) \tag{5.11}$$

To evaluate the integral in equation (5.11), spherical wave expansions of the test antenna and the probe antenna can be written as outgoing wave expressions in their respective coordinate systems as in equations (5,12), (5.13), (5.14) and (5.15).

$$\boldsymbol{E}_a(\boldsymbol{r}) = \sum_{n,m} a^{(4)}_{nm,a} \boldsymbol{M}^{(4)}_{nm}(\boldsymbol{r}) + b^{(4)}_{nm,a} \boldsymbol{N}^{(4)}_{nm}(\boldsymbol{r}) \tag{5.12}$$

$$\boldsymbol{H}_a(\boldsymbol{r}) = jY \sum_{n,m} b^{(4)}_{nm,a} \boldsymbol{M}^{(4)}_{nm}(\boldsymbol{r}) + a^{(4)}_{nm,a} \boldsymbol{N}^{(4)}_{nm}(\boldsymbol{r}) \tag{5.13}$$

$$\boldsymbol{E}_b(\boldsymbol{r}') = \sum_{n,m} a_{nm,b}^{(4)} \boldsymbol{M}_{nm}^{(4)}(\boldsymbol{r}') + b_{nm,b}^{(4)} \boldsymbol{N}_{nm}^{(4)}(\boldsymbol{r}') \tag{5.14}$$

$$\boldsymbol{H}_b(\boldsymbol{r}') = jY \sum_{n,m} b_{nm,b}^{(4)} \boldsymbol{M}_{nm}^{(4)}(\boldsymbol{r}') + a_{nm,b}^{(4)} \boldsymbol{N}_{nm}^{(4)}(\boldsymbol{r}') \tag{5.15}$$

All the fields given in equation (5.11) can be written in same coordinate system and spherical vector wave addition theorems are used in order to express $\boldsymbol{E}_b(\boldsymbol{r}')$ and $\boldsymbol{H}_b(\boldsymbol{r}')$ in terms of the wave function with the origin of *O*, which means changing the origin of $\boldsymbol{E}_b(\boldsymbol{r}')$ and $\boldsymbol{H}_b(\boldsymbol{r}')$ from *O'* to *O*. Coordinate translation followed by rotation is necessary for this purpose. (See Appendix A and Appendix B).

Translational additional theorem can be written as in equations (5.16) and (5.17) to perform translation between the coordinate systems with the origins of *O'* and *O''*.

$$\boldsymbol{M}_{nm}^{(4)}(\boldsymbol{r}') = \sum_{\nu=0}^{\infty} A_{\nu m}^{nm} \boldsymbol{M}_{\nu m}^{(1)}(\boldsymbol{r}'') + B_{\nu m}^{nm} \boldsymbol{N}_{\nu m}^{(1)}(\boldsymbol{r}'') \tag{5.16}$$

$$\boldsymbol{N}_{nm}^{(4)}(\boldsymbol{r}') = \sum_{\nu=0}^{\infty} A_{\nu m}^{nm} \boldsymbol{N}_{\nu m}^{(1)}(\boldsymbol{r}'') + B_{\nu m}^{nm} \boldsymbol{M}_{\nu m}^{(1)}(\boldsymbol{r}'') \tag{5.17}$$

Explicit form of translation coefficients, $A_{\nu m}^{nm}$ and $B_{\nu m}^{nm}$ are presented in Appendix A.

After the translation is performed, unprimed coordinate system can be obtained by rotating the double primed coordinate system by using Euler angles α, β and γ (See Appendix B) and rotational addition theorems stated in equations (5.18) and (5.19).

$$\boldsymbol{N}_{\nu m}^{(1)}(\boldsymbol{r}'') = \sum_{\mu=-\nu}^{\nu} D_{\mu m}^{(\nu)}(\alpha\beta\gamma) \boldsymbol{N}_{\nu\mu}^{(1)}(\boldsymbol{r}) \tag{5.18}$$

$$\boldsymbol{M}_{\nu m}^{(1)}(\boldsymbol{r}'') = \sum_{\mu=-\nu}^{\nu} D_{\mu m}^{(\nu)}(\alpha\beta\gamma)\ \boldsymbol{M}_{\nu\mu}^{(1)}(\boldsymbol{r}) \tag{5.19}$$

where

$$D_{\mu m}^{(\nu)}(\alpha\beta\gamma) = e^{jma} d_{\mu m}^{(\nu)}(\beta) e^{j\mu\gamma} \tag{5.20}$$

where rotational coefficient $d_{\mu m}^{(\nu)}(\beta)$ is given in Appendix B

By using translational and rotational addition theorems, fields of the probe antenna can be written in terms of coordinate system of the test antenna as:

$$\boldsymbol{E}_b(\boldsymbol{r}) = \sum_{\nu,\mu} a_{\nu\mu,b}^{(1)} \boldsymbol{M}_{\nu\mu}^{(1)}(\boldsymbol{r}) + b_{\nu\mu,b}^{(1)} \boldsymbol{N}_{\nu\mu}^{(1)}(\boldsymbol{r}) \tag{5.21}$$

$$\boldsymbol{H}_b(\boldsymbol{r}) = jY \sum_{\nu,\mu} b_{\nu\mu,b}^{(1)} \boldsymbol{M}_{\nu\mu}^{(1)}(\boldsymbol{r}) + a_{\nu\mu,b}^{(1)} \boldsymbol{N}_{\nu\mu}^{(1)}(\boldsymbol{r}) \tag{5.22}$$

where

$$a_{\nu\mu,b}^{(1)} = \sum_{n,m} D_{\mu m}^{(\nu)}(\alpha\beta\gamma) \left[a_{nm,b}^{(4)} A_{\nu m}^{nm} + b_{nm,b}^{(4)} B_{\nu m}^{nm} \right] \tag{5.23}$$

$$b_{\nu\mu,b}^{(1)} = \sum_{n,m} D_{\mu m}^{(\nu)}(\alpha\beta\gamma) \left[a_{nm,b}^{(4)} B_{\nu m}^{nm} + b_{nm,b}^{(4)} A_{\nu m}^{nm} \right] \tag{5.24}$$

Equation (5.11) reduces to equation (5.25) by inserting the fields of the test antenna stated in equations (5.12), (5.13) and fields of the probe antenna stated in equations (5.21) and (5.22).

$$\frac{n}{k^3}(-1)^m \sum_{n,m} \left[a^{(4)}_{nm,a}\, a^{(1)}_{n,-m,a} + b^{(1)}_{n,-m,a}\, a^{(4)}_{nm,a} \right] = P_B(r_0) \tag{5.25}$$

Multiply both side of equation (5.25) with $\left(D^{(n')}_{\mu' m'}(\alpha\beta\gamma)\right)^*$ and integrate over the ranges $0 \ll \alpha \ll 2\pi$, $0 \ll y \ll 2\pi$, $0 \ll b \ll 2\pi$, then equation 5.27 is obtained by orthogonality.

$$\int_{\gamma=0}^{2\pi}\int_{a=0}^{2\pi}\int_{\beta=0}^{\pi} D^{(n)}_{\mu m}(\alpha\beta\gamma)\left(D^{(n')}_{\mu' m'}(\alpha\beta\gamma)\right)^* \sin\beta\, d\beta da d\gamma = \frac{8\pi^2}{2n+1}\delta_{nn'}\delta_{mm'}\delta_{\mu\mu'} \tag{5.26}$$

$$\begin{aligned}(-1)^m \frac{8\pi^2 n}{k^2(2n+1)} &\left[a^{(4)}_{nm,a} A_{n\mu,b} + b^{(4)}_{nm,a} B_{n\mu,b}\right] \\ &= \int_{\gamma=0}^{2\pi}\int_{a=0}^{2\pi}\int_{\beta=0}^{\pi} e^{-j\mu a} d^{(n)}_{-m,\mu}(\beta) e^{jm\gamma}\, P_B(r_0)\, \sin\beta\, d\beta da d\gamma\end{aligned} \tag{5.27}$$

In equation (5.27), the coefficients $A_{n\mu,b}$ and $B_{n\mu,b}$ can be calculated by using (5.28) and (5.29) where $a^{(4)}_{\nu\mu,b}$ and $b^{(4)}_{\nu\mu,b}$ are the known receiving coefficients of the probe antenna and see Appendix A for $A^{\nu\mu}_{n\mu}$ and $B^{\nu\mu}_{n\mu}$.

$$A_{n\mu,b} = \sum_{\nu} a^{(4)}_{\nu\mu,b}\, A^{\nu\mu}_{n\mu} + b^{(4)}_{\nu\mu,b}\, B^{\nu\mu}_{n\mu} \tag{5.28}$$

$$B_{n\mu,b} = \sum_{\nu} a^{(4)}_{\nu\mu,b}\, B^{\nu\mu}_{n\mu} + b^{(4)}_{\nu\mu,b}\, A^{\nu\mu}_{n\mu} \tag{5.29}$$

Equation (5.27) is valid for any integer value of μ from $-n$ to n, for a given value of n and m, resulting in $2n+1$ linear equations. However, for a typical probe antenna only multipole coefficients with $\mu = \pm 1$ exist and equation (5.27) gives only two linear equations that can be used to solve the unknown test antenna coefficients a_{nm} and b_{nm}.

After the calculation of probe compensated multipole coefficients $a_{nm,a}^{(3)}$ and $b_{nm,a}^{(3)}$, far field $\boldsymbol{E}$ with probe compensation can be evaluated by inserting the compensated coefficients into equation (3.25) with the asymptotic form of vector wave functions $\boldsymbol{M}$ and $\boldsymbol{N}$.

5.2 Experimental Results for Spherical Probe Compensation

Mathematical derivation of the probe compensation is discussed in section 5.1 and the developed code is updated by adding this derivation for the probe compensation ability. This section focuses on the experimental validation of updated software by processing the near field data presented through Figure 5-2 to Figure 5-11. Also, output of updated software is compared with the SNIFT code. The probe antenna of "Antenna System Solutions" with the part number of $ASY - CWG - S - 058$ is used for the near filed measurements. The probe receiving coefficients provided by the manufacturer are used for the following probe compensation results.

Probe compensated output of the updated software with Trapezoid rule is presented in Figure 5-2 and Figure 5-4 for E_θ at $\phi = 0°$ and E_θ at $\phi = 90°$, respectively. These two figures show the compensation effect by comparing the far field E_θ with and without probe compensation. It is observed that, not negligible error on the main lobe and side lobes is obtained if no probe compensation is applied.

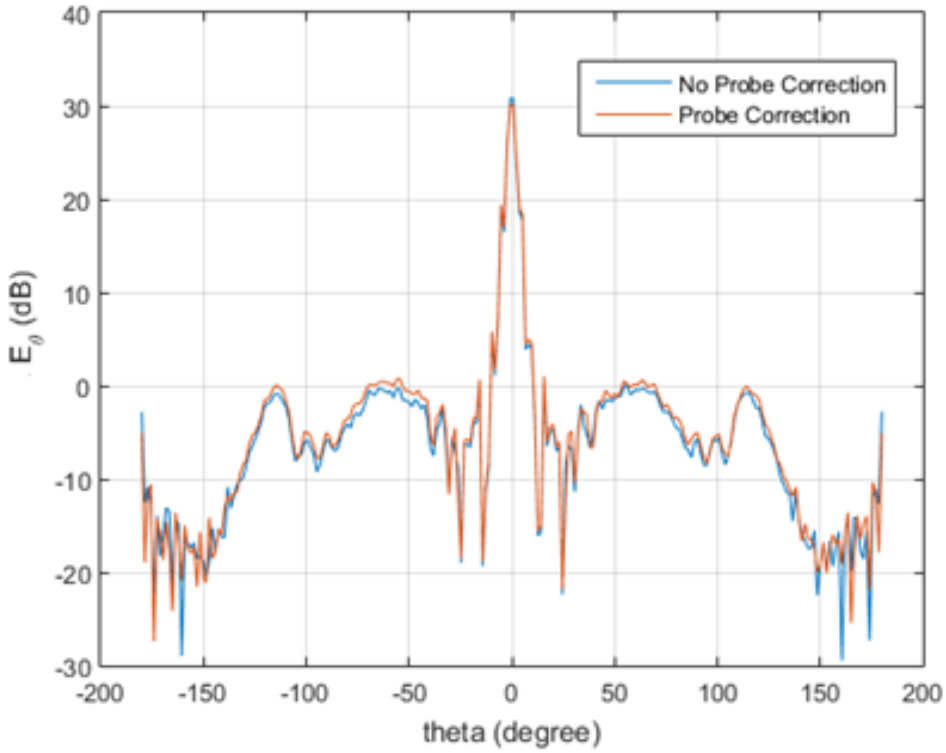

Figure 5-2: Comparison of far field E_θ calculated with and without probe compensation by using near field to far field transformation algorithm with Trapezoid quadrature at $\phi = 0^o$ and $f = 7.25\ GHz$

Probe compensation results of SNIFT code and developed software are presented in Figure 5-3 and Figure 5-5 for E_θ for $\phi = 0°$ and E_θ for $\phi = 90°$, respectively. It can be concluded that both results are in good agreement.

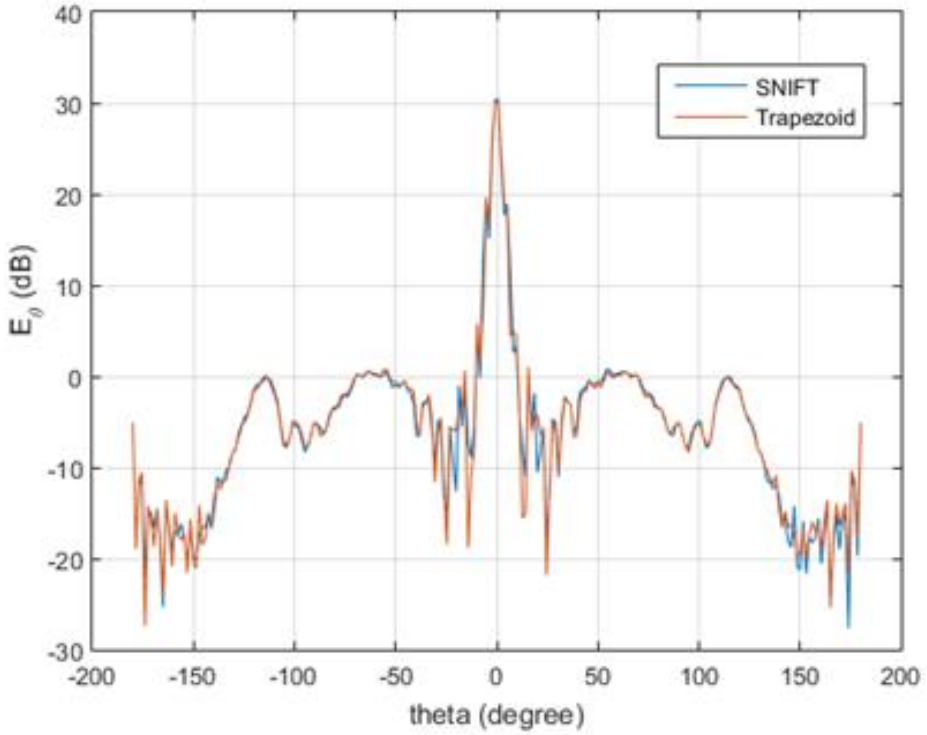

Figure 5-3: Comparison of the probe compensated far field E_θ with near field to far field transformation algorithm and SNIFT code at $\phi = 0^o$ and $f = 7.25\ GHz$

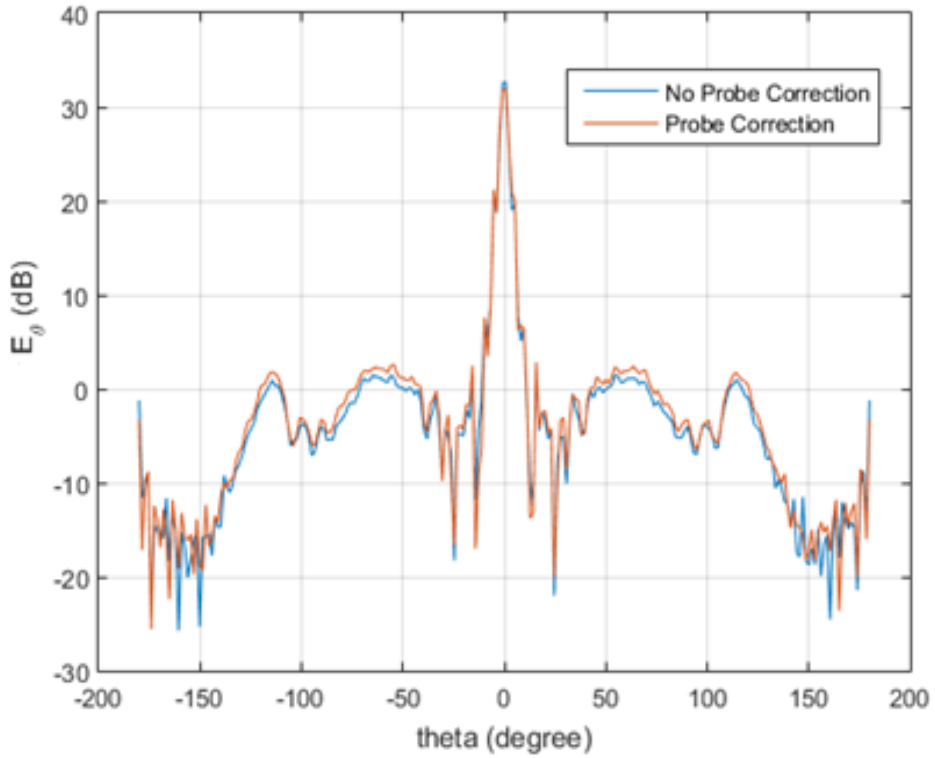

Figure 5-4: Comparison of far field E_θ calculated with and without probe compensation by using near field to far field transformation algorithm with Trapezoid quadrature at $\phi = 90^o$ and $f = 7.25\ GHz$

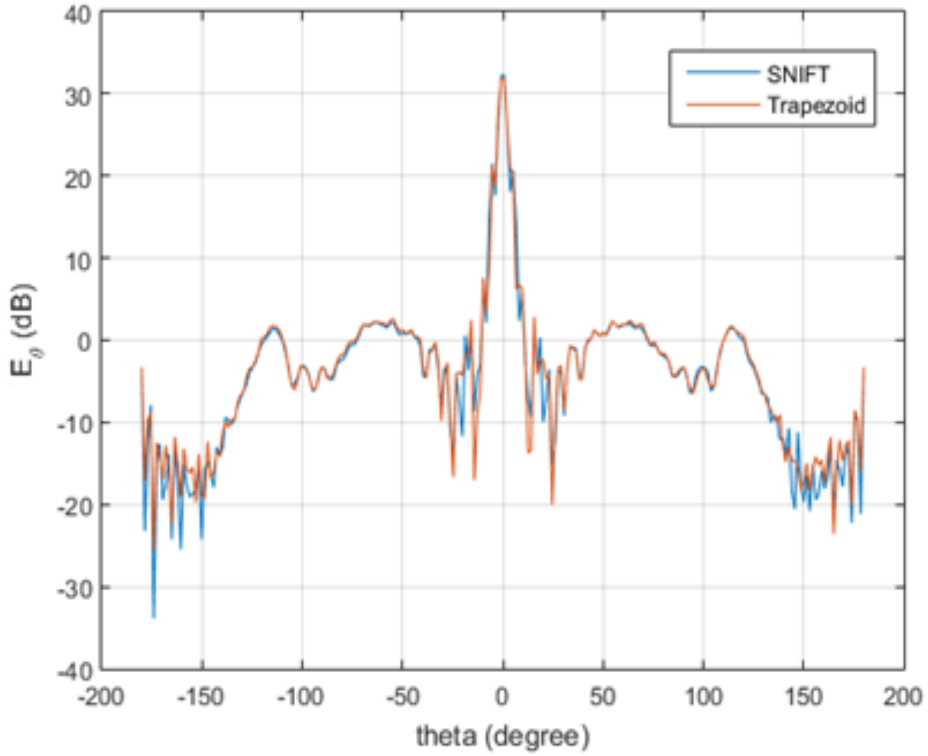

Figure 5-5: Comparison of the probe compensated far field E_θ with near field to far field transformation algorithm and SNIFT code at $\phi = 90^o$ and $f = 7.25\ GHz$

Probe compensation output of developed software with Trapezoid rule is presented in Figure 5-6 and Figure 5-8 for E_ϕ for $\phi = 0°$ and E_ϕ for $\phi = 90°$, respectively. Comparisons with SNIFT are presented in Figure 5-7 and Figure 5-9 which show that SNIFT and Trapezoid rule are in good agreement.

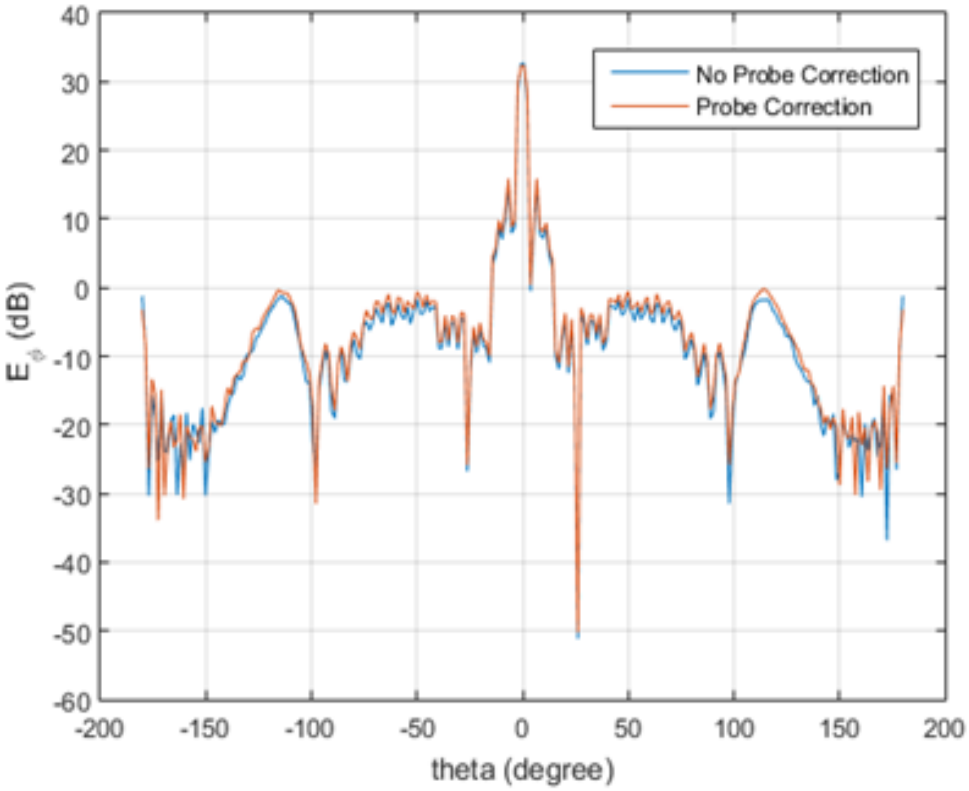

Figure 5-6: Comparison of far field E_ϕ calculated with and without probe compensation by using near field to far field transformation algorithm with Trapezoid quadrature at $\phi = 0^o$ and $f = 7.25\ GHz$

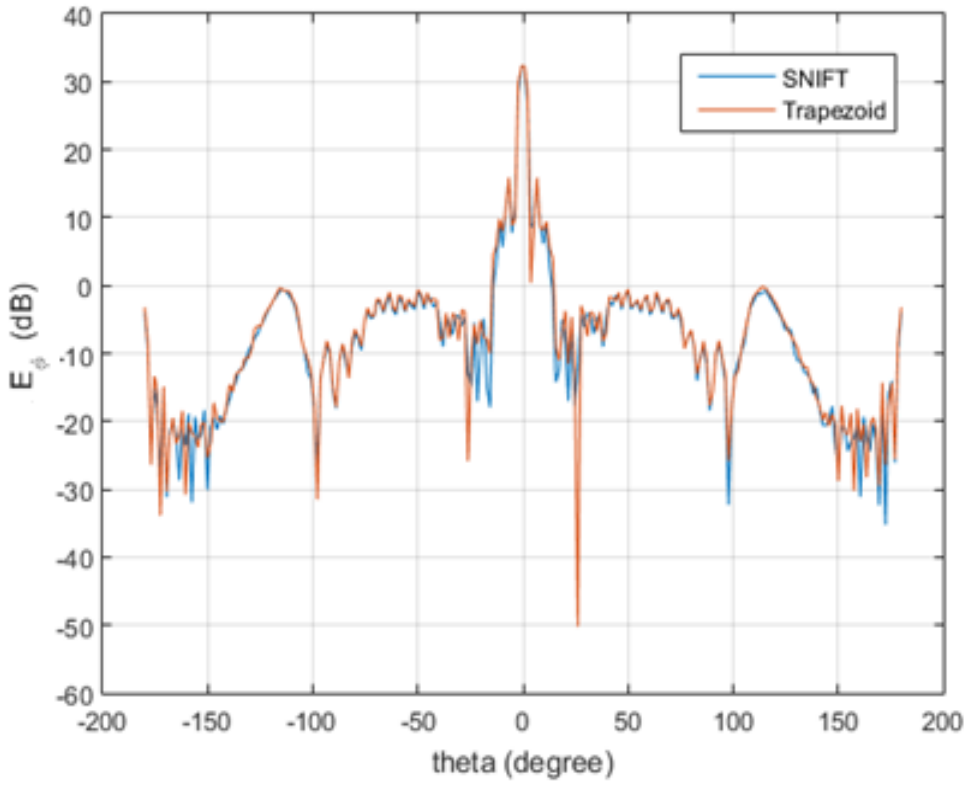

Figure 5-7: Comparison of the probe compensated far field E_ϕ with near field to far field transformation algorithm and SNIFT code at $\phi = 0^o$ and $f = 7.25\ GHz$

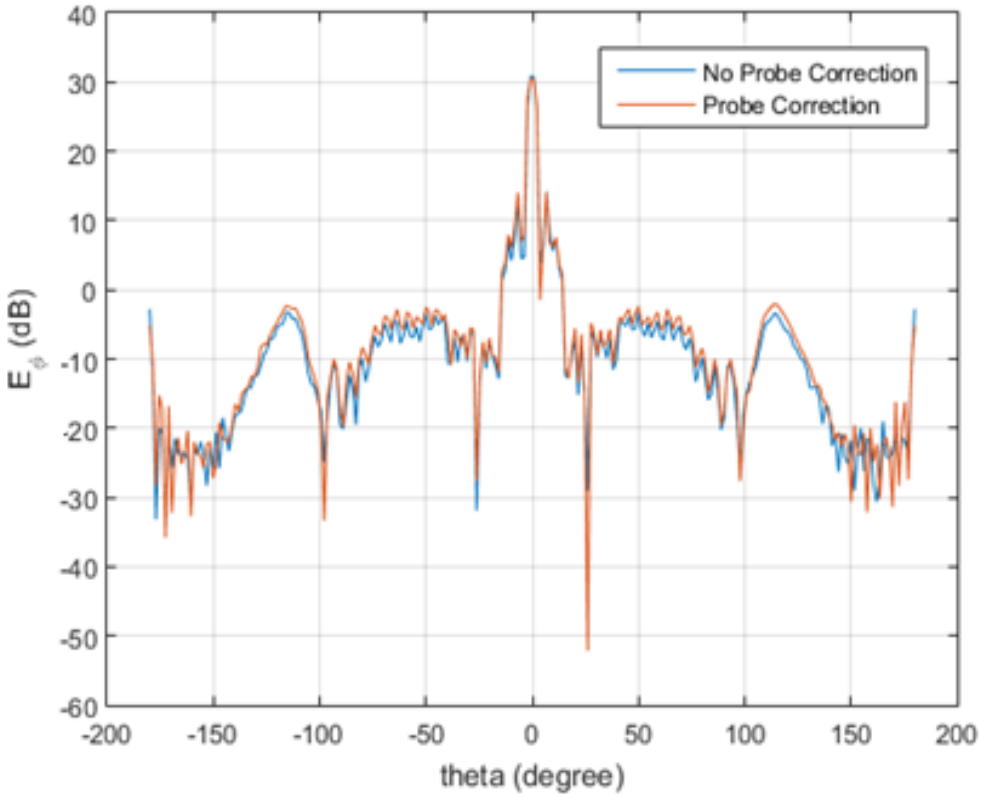

Figure 5-8: Comparison of far field E_ϕ calculated with and without probe compensation by using near field to far field transformation algorithm with Trapezoid quadrature at $\phi = 90^o$ and $f = 7.25\ GHz$

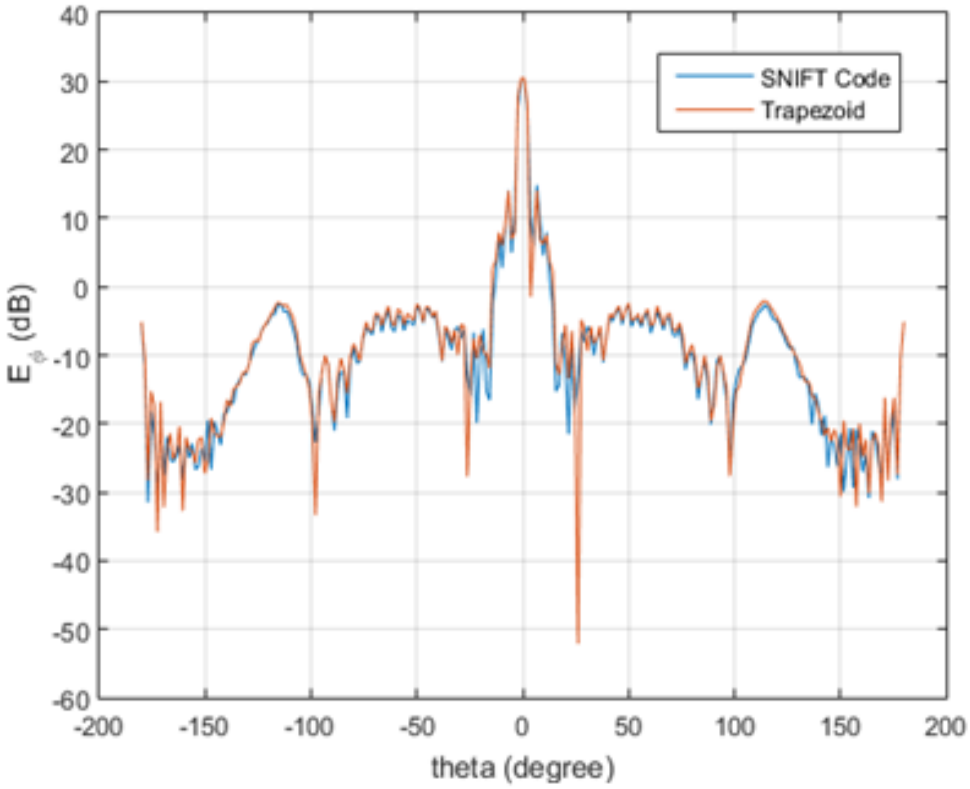

Figure 5-9: Comparison of probe compensated far field E_ϕ with near field to far field transformation algorithm and SNIFT code at $\phi = 90^o$ and $f = 7.25\ GHz$

Probe compensated far field E_θ pattern in $\phi = 0^o$ plane obtained by Simpson quadrature is given in Figure 5-10 which shows that error on sidelobes is observed without probe correction as in Trapezoid technique. Comparison of three output for probe compensation is presented in Figure 5-11 in which the agreement of SNIFT code and Trapezoid technique is revealed. The fast oscillations observed especially in the sidelobe region obtained by using the Simpson quadrature in the algorithm can be attributed to the inaccuracies of numerical calculations of Simpson quadrature.

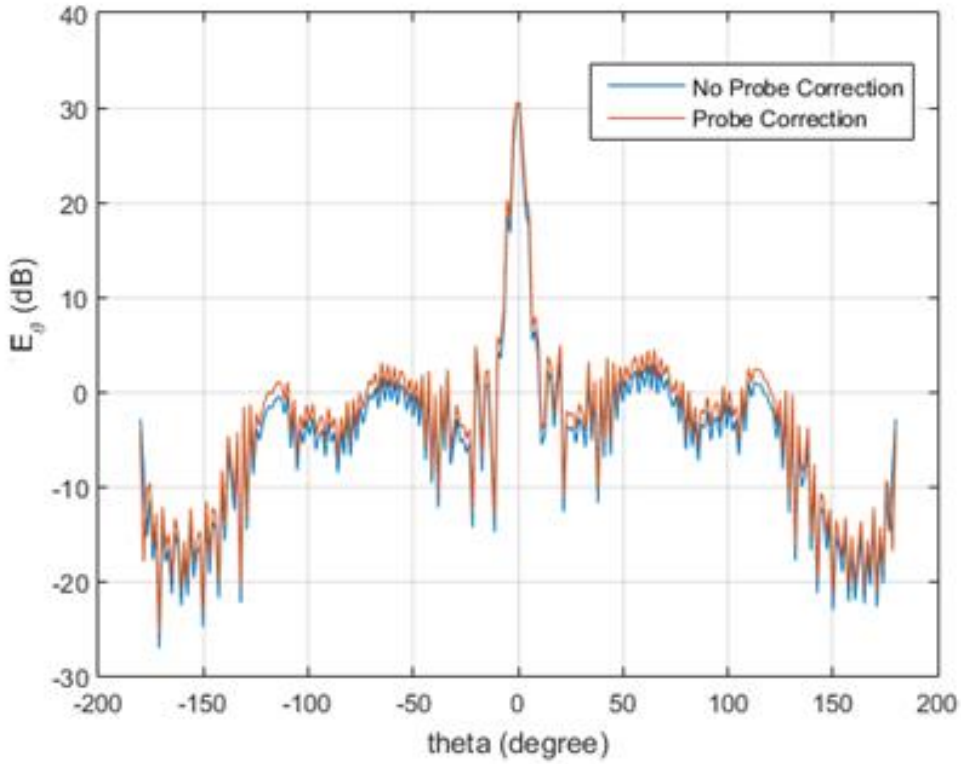

Figure 5-10: Comparison of far field E_θ calculated with and without probe compensation by using near field to far field transformation algorithm with Simpson quadrature at $\phi = 0^\circ$ and $f = 7.25\ GHz$

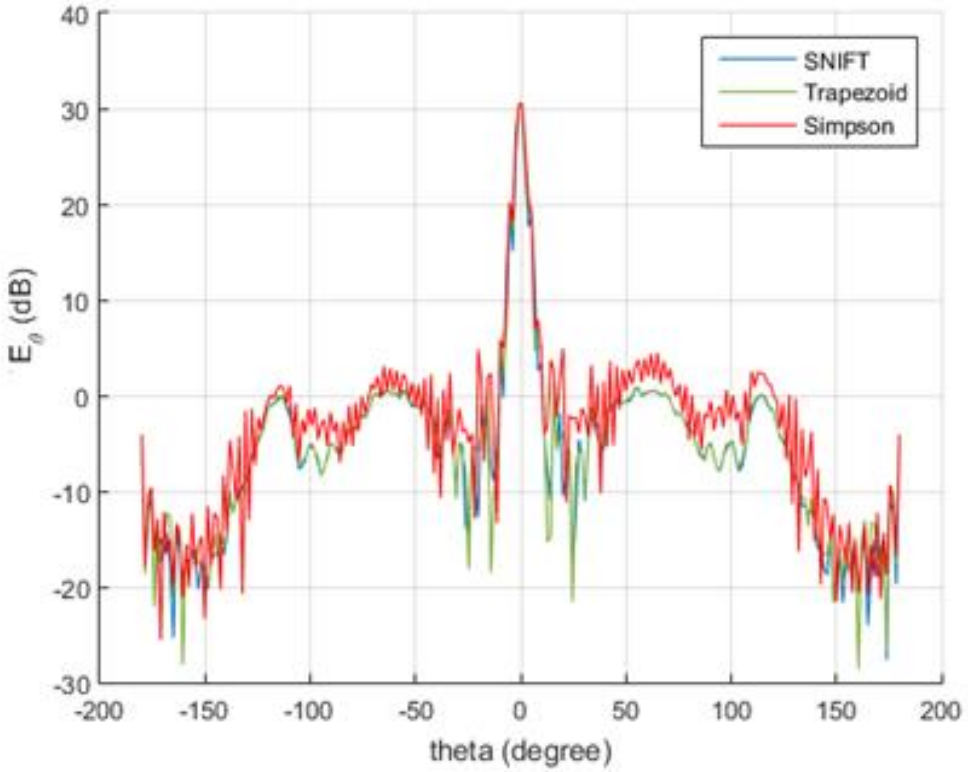

Figure 5-11: Comparison of probe compensated far field E_θ with near field to far field transformation algorithm, SNIFT code and Simpson at $\phi = 0^o$ and $f = 7.25\ GHz$

CHAPTER 6

CONCLUSION

In this thesis, the derivation and analysis of near field to far field transformation algorithm for spherical scanning is investigated. The main motivation is to use this algorithm for determining the far filed radiation of the antennas whose Rayleigh distances extends the laboratory scales.

Mathematical formulations for near field to far field transformation algorithm are studied and coded by using MATLAB® for different quadrature techniques and success of derived algorithm is tested by calculating the multipole coefficients of Hertzian dipole and plane wave with a known coefficient.

Spherical near field data acquired in METU anechoic chamber is processed with developed code and far field transformation of this data is performed with Trapezoid and Simpson rules to see which one fits better for this application. Also, MATLAB® code is run for different N to determine the most appropriate truncation order for the infinite sum of $\boldsymbol{E}$ field vector wave expansion and it is determined as $N = 2kr$.

Finally, probe compensation is studied to obtain the pure field of test antenna by eliminating the probe effect. Far field transform data with and without probe compensation is plotted to reveal the compensation effect.

Also, near field to far field transformation result of this study is compared with the SNIFT which is already being used by METU for far filed transformation of spherical scanning. This comparison is performed both the cases with and without probe compensation and it is observed that, SNIFT and this study are mostly in good agreement for Trapezoid rule. It is also observed that, Simpson is not a proper technique to approximate oscillating spherical Hankel functions.

For the future work, detail error analysis of quadrature methods can be studied and numerical optimization techniques could also be developed to decrease the calculation load for a huge data.

REFERENCES

[1] J.E Hansen (Editor), "*Spherical Near Field Antenna Measurements,* The Institution of Engineering and Technology, 1988.

[2] R. C. Wittmann and Carl F. Stubenrauch, "*Spherical Near-Field Scanning: Experimental and Theoretical Studies*" National Institute of Standards and Technology, pp. 26-46, Dec 1991.

[3] A. Jerry "*Handbook of Mathematical Formulas and Integration*", Elsevier Inc, pp. 289-315, 2008.

[4] F. Jensen "*Electromagnetic Near Field Far Field Correlations*", Ph.D. dissertation, The Technical University of Denmark, Lyngby, pp. 33-43, July 1970

[5] C. A. Balanis, "*Advanced Engineering Electromagnetics*", A. John Wiely & Sons Inc., pp. 121-126, 1989.

[6] A. R. Edmonds "*Angular Momentum in Quantum Mechanics*", Princeton University Press, pp. 6-8, 1974.

[7] M. Abramowitz (Editor), I. A. Stegun (Editor), *"Handbook of Mathematical Functions with Formulas, Graphs, and Mathematical Tables*", pp. 331-355, 1968.

[8] A. D. Polyanin, Alexander V. Manzhirow, "*Handbook of Mathematics for Engineers and Scientists"*, Chapman & Hall/CRC Inc. of Taylor & Francis Group, LLC, pp. 962-967, 2007.

[9] C. A. Balanis, "*Antenna Theory - Analysis and Design*", A. John Wiely & Sons Inc., Third Edition, 2005.

[10] R. Harrington*, "Time-Harmonic Electromagnetic Fields"*, IEEE Press Classical Reissue, IEEE Inc, pp. 264-276, 2001.

[11] J.E. Hansen, F. Jensen, "*Spherical Near-Field Scanning at The Technical - University of Denmark"*, IEEE Transactions on Antennas and Propagation, Vol. 36, No. 6, June 1988.

[12] P. F. Wacker," Non-*Planar Near Field Measurements: Spherical Scanning*", Electromagnetic Division Institute for Basic Standards National Bureau of Standards Boulder, pp. 25-39, June 1975.

[13] S. Koc, Song, J; Chew, WC, "*Error analysis for the numerical evaluation of the diagonal forms of the scalar spherical addition theorem*", Society for Industrial and Applied Mathematics, 1999.

[14] J.M. Song, W.C Chew, "*Multilevel Fast Multipole Algorithm for Solving Combined Field Integral Equation of Electromagnetic Scattering*", Department of Electrical and Computer Engineering University of Illinois, Urbana, March 1995.

[15] W. C. Chew, Tie Jun Cui, Jiming M. Song, *"A FAFFA-MLFMA Algorithm for Electromagnetic Scattering"*, IEEE Transactions on Antennas and Propagation, Vol. 50, No. 11, November 2002.

[16] J. H. Brunning, Yuent T. LO, "*Multiple Scattering of EM Waves by Spheres Part I-Multipole Expansion and Ray-Optical Solutions"*, IEEE Transactions on Antennas and Propagation, Vol. AP-19, No. 3, May 1971.

[17] H. Oraizi, H. Soleimani *"Optimum pattern synthesis of non-uniform spherical arrays using the Euler rotation"*, The Institution of Engineering and Technology Microwaves, Antennas & Propagation, 2014.

[18] A.C. Newell, *"Near Field Antenna Measurement Theory, Planar, Cylindrical and Spherical"*, Nearfield Systems Inc., 2009.

[19] A.D. Yaghjlan, *"An Overview of Near-Field Antenna Measurements"* IEEE Transactions on Antennas and Propagation, Vol. AP-34, No. 1, January 1986.

[20] Ing. Roman TKADLEC, Doctoral Degree Programme, Dept. of Radio Electronics, FEEC, BUT, *"Near Field Antenna Measurement"*.

[21] S. Sencer Koç, "*Use of Spherical Vector Wave Functions in Near Field Measurements and Calculations"*, pp. 27-36, December 1987.

[22] R. S. Elliott, "Antenna *Theory and Design"*, pp. 38-41, IEEE Inc., 2003.

[23] S. Koç, *"Lecture Notes on EE 521 Analytical Methods for Electromagnetic Theory*", Middle East Technical University, Electrical and Electronics Engineering Department.

[24] E. J. Paez, J. P. Regina, M. D. Sandoval, P. D. Pino, C. D. Tremola, B. M. Azpurua, *"Theoretical and Practical Validation Tests for a Near-Field to Far-Field Transformation Algorithm Using Spherical Wave Expansion"*, Rev. Tec. Ing. Univ. Zulia, Vol. 35, Nº 1, 109 - 118, 2012.

[25] P. J. Davis, P. Rabinowitz, "Methods of Numerical Integration", Dover Publications, Inc., pp. 51-68, 2007.

[26] A. Frandsen, "*SNIFT / ROSCOE User Guide and Manuel", TICRA, Copenhagen, Denmark*, 2011

[27] Krishna THAPA, *"Calculation of Highly Oscillatory Integrals by Quadrature Methods"*, Texas A&M University, pp. 2-4, May2012.

[28] D.T. Paris, W. M. Leach, Edward B. Joy, *"Basic Theory of Probe Compensation Near Field Measurements"*, IEEE Transactions on Antennas and Propagation, Vol. AP-26, No. 3, May1978.

[29] J.D. Jackson, "Classical Electrodynamics" John Willey & Sons, New York, 1975

APPENDIX

A. COORDINATE TRANSFORMATION

This section is based on [21]

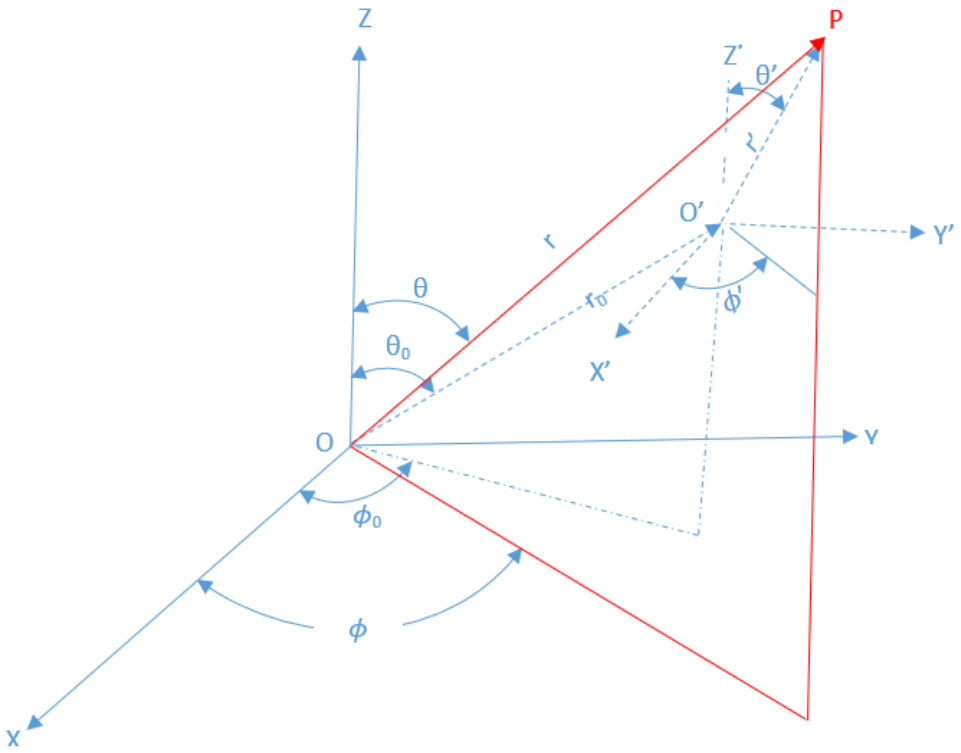

Figure A- 1: Coordinate transformation geometry

$$\begin{bmatrix} \boldsymbol{a}_{x'} \\ \boldsymbol{a}_{y'} \\ \boldsymbol{a}_{z'} \end{bmatrix} = \begin{bmatrix} q_{11} & q_{12} & q_{13} \\ q_{21} & q_{22} & q_{23} \\ q_{31} & q_{32} & q_{33} \end{bmatrix} \begin{bmatrix} \boldsymbol{a}_{x} \\ \boldsymbol{a}_{y} \\ \boldsymbol{a}_{z} \end{bmatrix} \tag{A.1}$$

(A.1) is coordinate rotation matrix.

Rotation about z-axis

$$\mathrm{P'} = \begin{bmatrix} \cos\Phi_0 & \sin\Phi_0 & 0 \\ -\sin\Phi_0 & \cos\Phi_0 & 0 \\ 0 & 0 & 1 \end{bmatrix} \tag{A.2}$$

Rotation about x-axis

$$P'' = \begin{bmatrix} 1 & 0 & 0 \\ 0 & \cos\theta_0 & \sin\theta_0 \\ 0 & -\sin\theta_0 & \cos\theta_0 \end{bmatrix} \tag{A.3}$$

Rotation about y-axis

$$\mathrm{P'''} = \begin{bmatrix} \cos x_0 & 0 & -\sin x_0 \\ 0 & 1 & 0 \\ \sin x_0 & 0 & \cos x_0 \end{bmatrix} \tag{A.4}$$

If only translation is involved, the coefficients A_{mv}^{mn} and B_{mv}^{mn} are given by;

$$A_{v\mu}^{nm} = (-1)^{\mu} \sum_{p} a(m,n|\mu,v|p)\, a(n,v,p)\, P_p^{m-\mu}(\cos\theta_0)\, e^{j(m-\mu)\phi_0} \begin{Bmatrix} z_p^{(a)}(kr_0)\,, r' \le r_0 \\ j_p(kr_0)\,, r' \ge r_0 \end{Bmatrix} \tag{A.5}$$

$$B_{v\mu}^{nm} = (-1)^{\mu+1} \sum_{p} a(m,n|\mu,v|p,p-1)\, b(n,v,p)\, P_p^{m-\mu}(\cos\theta_0)\, e^{j(m-\mu)\phi_0} \begin{Bmatrix} z_p^{(a)}(kr_0)\,, r' \le r_0 \\ j_p(kr_0)\,, r' \ge r_0 \end{Bmatrix} \tag{A.6}$$

$$a(n,\nu\,,p) = j^{\nu+p-n}$$

$$\left[\frac{2\nu\ (\nu\ +1)(2\nu\ +1)+(\nu+1)(n-\nu\ +p+1)(n+\nu\ -p)}{2\nu\ (\nu\ +1)}\right. \tag{A.7}$$
$$\left. -\frac{\nu\ (\nu\ -n+p+1)(n+\nu\ +p+2)}{2\nu\ (\nu\ +1)}\right]$$

$$b(n,\nu\,,p) = j^{\nu+p-n}$$
$$\left[[(n+\nu\ +p+1)(n-\nu\ +p)(n-\nu\ +p)(n+\nu\ -p+1)]^{1/2}\right]\frac{2\nu\ +1}{2\nu\ (\nu\ +1)} \tag{A.8}$$

Summation over p is finite covering the range $|n-v|, |n-v|+2, \dots, n+v$ and includes $1+min\{n,v\}$ terms. The coefficients $a(m,n|\mu,\nu\,|p)$ are defined by the linearization expansion;

$$P_n^m(x)\,P_\nu^\mu(x) = \sum_p a(m,n|\mu,\nu\,|p)\ P_p^{m+\mu}(x) \tag{A.9}$$

When a translation along the z-axis by a distance r_0 is required the addition, problem takes the following simpler form;

$$\boldsymbol{M}_{nm}^{(a)}(\boldsymbol{r}) = \sum_{\nu\,=\min\,(1,m)}^{\infty} A_{m\nu}^{mn}\ \boldsymbol{M}_{m\nu}^{(1)}\ (\boldsymbol{r}) + B_{m\nu}^{mn}\ \boldsymbol{N}_{m\nu}^{(1)}\ (\boldsymbol{r}\,) \tag{A.10}$$

$$\boldsymbol{N}_{nm}^{(a)}(\boldsymbol{r}) = \sum_{\nu\,=\min\,(1,m)}^{\infty} A_{m\nu}^{mn}\ \boldsymbol{N}_{m\nu}^{(1)}\ (\boldsymbol{r}) + B_{m\nu}^{mn}\ \boldsymbol{M}_{m\nu}^{(1)}\ (\boldsymbol{r}) \tag{A.11}$$

Which applies translation from O to O'. When translation from O to O', $A_{m\nu}^{mn}$ and $B_{m\nu}^{mn}$ are predicted by the factors $(-1)^{m+\nu}$ and $(-1)^{m+\nu+1}$ respectively. The translation coefficients, which can be obtained from more general formulas above are given by;

$$A_{m\nu}^{mn} = (-1)^m j^{\nu-n} \frac{2\nu+1}{2\nu(\nu+1)} \sum_p j^p \left[n(n+1) + \nu(\nu+1) - p(p+1)\right] \quad \text{(A.12)}$$

$$a(m,n|-m,\nu|p) \begin{Bmatrix} Z_p^{(a)}(kr_0)\,, r \leq r_0 \\ j_p(kr_0)\,, r \geq r_0 \end{Bmatrix} \quad \text{(A.13)}$$

$$B_{m\nu}^{mn} = (-1)^m j^{\nu-n} \frac{2\nu+1}{2\nu(\nu+1)} \sum_p j^{-p} \ (-2jmkr_0) \quad \text{(A.14)}$$

As stated, above recursion relation for the $a(.)$ exists and is given by;

$$\alpha_{p-3}\, a_{p-4} - \left(\alpha_{p-2} + \alpha_{p-1} + 4m^2\right) a_{p-2} + \alpha_p\, a_p = 0 \quad \text{(A.15)}$$

$$\alpha_p = \frac{[(n+\nu+1)^2 - p^2][p^2 - (n-\nu)^2]}{4p^2 - 1} \quad \text{(A.16)}$$

$$a_{n+\nu} = \frac{(2n-1)!!\,(2\nu-1)!!}{(2n+2\nu-1)!!} \frac{(n+\nu)!}{(n-m)!\,(\nu+m)!} \quad \text{(A.17)}$$

$$a_{n+\nu-2} = \frac{(2n+2\nu-3)}{(2n-1)(2\nu-1)(n+\nu)} \left[n\nu - m^2(2n+2\nu-1)\right] a_{n+\nu} \quad \text{(A.18)}$$

where $(2t-1)!! = (2t-1)\,(2t-3)\ \ldots 3.1;\ (-1)!! = 1$

B. COORDINATE ROTATIONS

This section is based on [21]

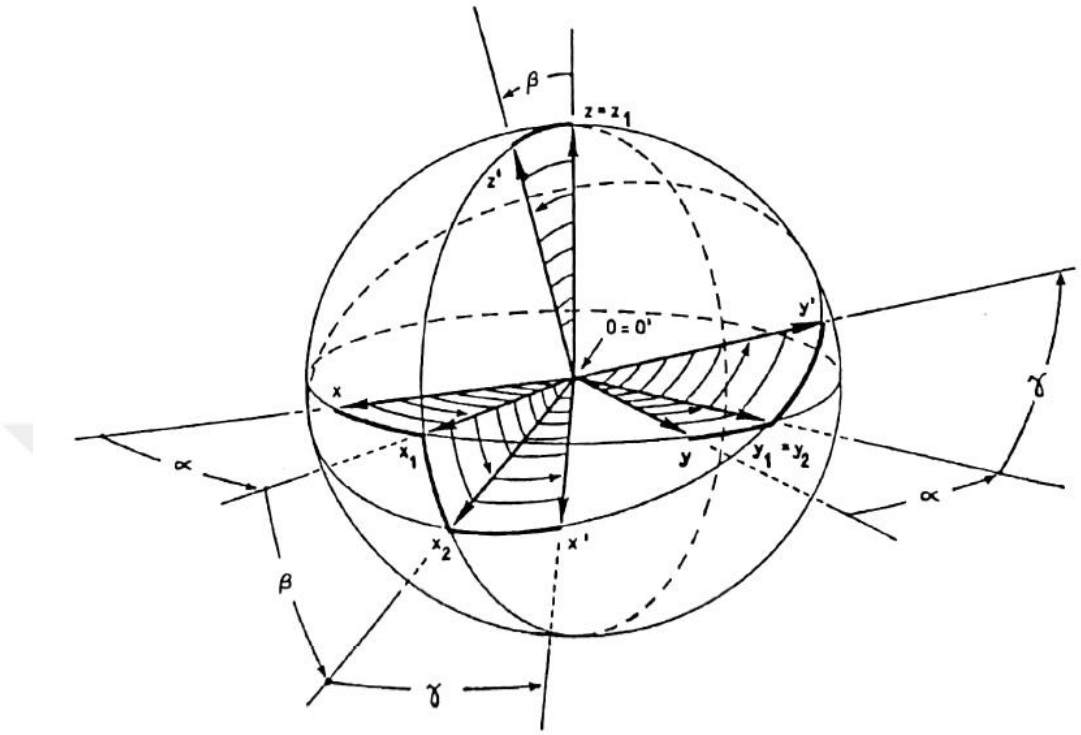

Figure B- 1: Coordinate rotation geometry

It is extremely simple to describe the addition theorems for $\boldsymbol{M}_{nm}$and $\boldsymbol{N}_{nm}$under coordinate rotations.

$$Y_{nm}(\theta,\phi) = \sum_{\mu=-n}^{n} Y_{nm}\,(\theta^{*}\phi^{*})\; D_{\mu m}^{(n)}(\alpha\beta\gamma) \tag{B.1}$$

$$Y_{nm} = \left[\frac{2n+1}{4\pi}\,\frac{(n-m)!}{(n+m)!}\right]^{\frac{1}{2}} P_n^m(\cos\theta)e^{jm\phi} \tag{B.2}$$

The conversion used is that the Euler angles α,β,γ correspond to $R_{z,}\,R_{Y,}R'_z$ rotation angles, respectively.

$$D_{\mu m}^{(n)} = e^{jma}\, d_{\mu m}^{(n)}(\beta)\, e^{j\mu\gamma} \tag{B.3}$$

where

$$d_{\mu m}^{(n)}(\beta) = \left[\frac{(n+\mu)!}{(n+m)!}\frac{(n-\mu)!}{(n-m)!}\right]^{1/2}$$

$$\sum_{\sigma}\binom{n+m}{n-\mu-\sigma}\binom{n-m}{\sigma}(-1)^{n-\mu-\sigma}\left(\cos\frac{\beta}{2}\right)^{2\sigma+\mu+m}\left(\sin\frac{\beta}{2}\right)^{2n-2\sigma-\mu-m} \tag{B.4}$$

$$u_{n\mu}^{a}(r,\theta,\phi) = \sum_{\mu=-n}^{n} D_{\mu m}^{(n)}(\alpha\beta\gamma)\ (r',\theta',\phi') \tag{B.5}$$

$$\boldsymbol{M}_{nm}^{a}(r,\theta,\phi) = \nabla u_{n\mu}^{a}(r,\theta,\phi)\ \times \boldsymbol{r} = \sum_{\mu=-n}^{n} D_{\mu m}^{(n)}(\alpha\beta\gamma)\,\boldsymbol{M}_{nm}^{a}\ (r',\theta',\phi') \tag{B.6}$$

$$\boldsymbol{N}_{nm}^{(4)}(\boldsymbol{r}') = \sum_{\nu=0}^{\infty} A_{\nu m}^{nm}\,\boldsymbol{N}_{\nu m}^{(1)}(\boldsymbol{r}'') + B_{\nu m}^{nm}\,\boldsymbol{M}_{\nu m}^{(1)}(\boldsymbol{r}'') \tag{B.7}$$

$$\boldsymbol{M}_{nm}^{(4)}(\boldsymbol{r}') = \sum_{\nu=0}^{\infty} A_{\nu m}^{nm}\,\boldsymbol{M}_{\nu m}^{(1)}(\boldsymbol{r}'') + B_{\nu m}^{nm}\,\boldsymbol{M}_{\nu m}^{(1)}(\boldsymbol{r}'') \tag{B.8}$$

$$\boldsymbol{E}_{b}(\boldsymbol{r}) = \sum_{\nu,\mu} a_{\nu\mu,b}^{(1)}\boldsymbol{M}_{\nu\mu}^{(1)}(\vec{r}) + b_{\nu\mu,b}^{(1)}\,\boldsymbol{N}_{\nu\mu}^{(1)}(\boldsymbol{r}) \tag{B.9}$$

$$\boldsymbol{H}_{b}(\boldsymbol{r}) = jY\sum_{\nu,\mu} b_{\nu\mu,b}^{(1)}\boldsymbol{M}_{\nu\mu}^{(1)}(\boldsymbol{r}) + a_{\nu\mu,b}^{(1)}\boldsymbol{N}_{\nu\mu}^{(1)}(\boldsymbol{r}) \tag{B.10}$$